

# Isotopic analysis of 295 MeV proton scattering off $^{204,206,208}\text{Pb}$ for improvement of neutron densities and radii

Yoshiko Kanada-En'yo

*Department of Physics, Kyoto University, Kyoto 606-8502, Japan*

A new method of reaction analysis for proton elastic scattering is proposed, combining systematic analyses of nuclear structure and reactions in a series of isotopes. This method is applied to  $^{204}\text{Pb}(p,p)$ ,  $^{206}\text{Pb}(p,p)$ , and  $^{208}\text{Pb}(p,p)$  at  $E_p = 295$  MeV to obtain improved neutron densities and radii from experimental cross section data. The reaction calculation is performed according to the relativistic impulse approximation using the modified Murdock and Horowitz model with density-dependent effective  $NN$  interaction. Analysis of Pb isotopes is performed using theoretical densities given by the relativistic Hartree-Bogoliubov and nonrelativistic Skyrme Hartree-Fock-Bogoliubov calculations and the experimental density extracted from the  $(p,p)$  data at 295 MeV. The isotopic ratios ( $R(\sigma)$ ) of the  $^A\text{Pb}(p,p)$ -to- $^{208}\text{Pb}(p,p)$  cross sections are analyzed in connection with the isotopic differences ( $D(\rho_n)$  and  $D(r_n)$ ) in neutron densities ( $\rho_n(r)$ ) and radii ( $r_n$ ) between  $^A\text{Pb}$  and  $^{208}\text{Pb}$ . A hole-model analysis is performed, assuming  $^{204}\text{Pb}$  and  $^{206}\text{Pb}$  as a  $^{208}\text{Pb}$  core and neutron holes to clarify the one-to-one correspondence between isotopic structure properties such as  $D(\rho_n)$  and  $D(r_n)$  and the isotopic cross-section ratio. By fitting  $R(\sigma)$ , the values of  $D(\rho_n)$  and  $D(r_n)$  are extracted from the experimental  $(p,p)$  cross section data with less uncertainty of the structure and reaction models. The isotopic neutron radius difference between  $^{206}\text{Pb}$  and  $^{208}\text{Pb}$  was obtained as  $D(r_n) = -0.012$  fm with an acceptable range of  $D(r_n) = -0.03 \sim -0.006$  fm.

## I. INTRODUCTION

The neutron skin thickness  $\Delta r_{np}$  in  $N > Z$  nuclei—which is defined as the difference between the root-mean-square (rms) point-proton ( $r_p$ ) and neutron ( $r_n$ ) radii  $\Delta r_{np} = r_n - r_p$ —has long been intensively investigated through experimental and theoretical studies. The experimental determination of  $\Delta r_{np}$  in double closed nuclei such as  $^{48}\text{Ca}$ ,  $^{208}\text{Pb}$ , and  $^{132}\text{Sn}$  is an urgent issue for accessing to the neutron matter EOS via the connection between  $\Delta r_{np}$  and the symmetry energy parameters [1–3]. Various experimental approaches have been applied for measuring  $\Delta r_{np}$ . For stable nuclei, point-proton radii and density distributions can be precisely determined from the charge radii and form factors measured by electric probes such as the isotope shift of  $x$  rays and electron scattering. However, measuring neutron radii is relatively difficult; hence, the  $\Delta r_{np}$  data still contain large experimental errors. Many experimental efforts have been made to determine the  $r_n$  of  $^{208}\text{Pb}$  by measuring proton elastic scattering [4, 5],  $x$ -ray cascade from antiprotonic atoms [6], parity-violating electron scattering [7], and pionic probes [8, 9]. The electric dipole polarization measured by polarized proton inelastic scattering [10] is an alternative approach for determining  $\Delta r_{np}$  [11].

The observed  $\Delta r_{np}$  data were used to extract information for the neutron matter EOS based on nuclear density functional theory (DFT) by comparing the data with theoretical predictions of  $\Delta r_{np}$  calculated using a variety of relativistic and nonrelativistic energy density functionals. In extracting infinite matter properties from nuclear observables using DFT, it is essential to reduce model dependences mainly originating in finite-size effects such as surface contributions and shell effects in  $\Delta r_{np}$  [12].

Proton elastic scattering is a useful tool for investi-

gating the detailed profile of the neutron-density distribution as used for nuclei in wide mass-number regions. The neutron-density distribution of  $^{208}\text{Pb}$  was extracted from the  $(p,p)$  data at 800 MeV [13–15], 650 MeV [4], and 295 MeV [5]. For reaction analyses of proton elastic scattering at several hundreds of MeV, a reaction model based on the relativistic impulse approximation (RIA) framework with meson-exchange effective  $NN$  interactions was proposed by Murdock and Horowitz (MH model); this model is based on globally fitting the  $(p,p)$  data in the  $E_p = 100$ –400 MeV energy range [16–18]. The RIA code with the MH model has been widely used to investigate neutron density based on  $(p,p)$  data. Later, an improved version, the density-dependent MH model (ddMH) was proposed by Sakaguchi and his collaborators, introducing density dependences of the effective  $NN$  interaction [5, 19, 20]. The ddMH model was finely calibrated to 295 MeV proton elastic scattering off  $^{58}\text{Ni}$  at scattering angles of  $\theta_{\text{c.m.}}$  up to  $\sim 50^\circ$ , and proton elastic scattering off the Sn [20], Pb [5], and Ca [21] isotopes was successfully described. By taking high-quality measurements of the proton elastic scattering off  $^{204}\text{Pb}$ ,  $^{206}\text{Pb}$ , and  $^{208}\text{Pb}$  at 295 MeV, the neutron densities were extracted via reaction analysis using RIA with the ddMH model and the  $r_n$  values in a series of Pb isotopes were obtained [5].

However, the  $r_n$  values of the Pb isotopes determined by the  $(p,p)$  data still contain significant experimental errors, mainly because of the large uncertainty of the extracted neutron density in the internal region, to which proton scattering at several hundreds of MeV is insensitive [22]. To avoid the uncertainty in  $r_n$  extracted from the  $(p,p)$  data, a new method based DFT was proposed to evaluate the symmetry-energy parameters by comparing the surface-neutron-density profile of the theoretical predictions with the experimental density extracted from

the data instead of  $r_n$ , and it was applied to analysis of the  $^{208}\text{Pb}$  and  $^{48}\text{Ca}$  densities [23]. Alternatively, a more direct approach between the data and matter information through a comparison of the experimental  $(p,p)$  cross sections with theoretical predictions obtained by reaction calculations using DFT densities may be worth considering.

Our aim in this paper is to propose a new reaction analysis method for the proton elastic scattering measured in a series of isotopes to obtain improved neutron density and radii from the data. Because of the similarities between neighboring nuclei, a perturbative treatment is possible, and relative differences between neighboring nuclei can be easily detected with less uncertainty in principle. Therefore, a systematic analysis combining the data in a series of neighboring isotopes can be a better tool than independent analyses because it can significantly reduce systematic errors. A similar concept is often used, for instance, to determine of charge-radius differences by measuring the isotope shift of  $x$  rays. For proton scattering, an isotopic analysis was performed to discuss neutron-density differences [14]; however, an important innovation of the present work is that it combines the isotopic properties of nuclear structure with those of nuclear reaction—that is an isotopic analysis of the scattering cross sections is performed to extract structural differences between isotopes via reaction calculations. For electron elastic scattering, an isotopic analysis of the cross sections has been performed to discuss the isotopic difference in the charge radius [24]; however, its application is limited. Little work has been done on proton elastic scattering, except for a brief discussion of the isotopic cross-section ratio and size scaling of the proton-nucleus potential [25].

In this paper, I propose a new approach using isotopic analysis of the proton elastic scattering cross sections. Based on isotopic systematics in nuclear structures and reactions. In the ground state of even-even nuclei, the nuclear structure changes smoothly in a series of isotopes without drastic changes, other than crossing a shell gap or phase transition for nuclear deformation. Moreover, the reaction processes of neighboring isotopes at the same energy should be similar, provided that the projectile energy is high enough to neglect the mass-number dependence of higher-order effects such as channel-coupling effects in the proton scattering. Another advantage of this approach is that, experimental systematic errors can be significantly reduced using the observed data in a series of isotopes measured experimentally with the same setup in the same facility.

For isotopic analysis, the reaction calculations of  $^{204}\text{Pb}(p,p)$ ,  $^{206}\text{Pb}(p,p)$ , and  $^{208}\text{Pb}(p,p)$  at  $E_p = 295$  MeV were performed via RIA calculation using the ddMH model in the same way as was done in the analysis of Ref. [5]. As for the target densities in the reaction calculation, the theoretical densities of the Pb isotopes obtained by relativistic Hartree-Bogoliubov (RHB) and nonrelativistic Skyrme Hartree-Fock-Bogoliubov (SHFB)

calculations of spherical nuclei and the experimental density extracted by fitting the  $(p,p)$  data are used. The isotopic neutron density and radius differences and the isotopic cross-section ratios of  $^{204}\text{Pb}$ ,  $^{206}\text{Pb}$ , and  $^{208}\text{Pb}$  are investigated. A detailed analysis is performed by introducing a hole model of  $^{204}\text{Pb}$  and  $^{206}\text{Pb}$  as a  $^{208}\text{Pb}$  core and neutron holes, the sensitivity of the cross sections to surface-neutron densities is clarified. Through the hole-model analysis, the improved neutron densities and radii are obtained by fitting the isotopic cross-section ratio obtained from the  $(p,p)$  data. The uncertainty in the structure and reaction models is discussed.

This paper is organized as follows. The structure and reaction calculations are described and the obtained results of the Pb isotopes are presented in Sec. II. Isotopic analysis using the theoretical and experimental densities is performed in Sec. III, and the hole-model analysis is done in Sec. IV. In Sec. V, improved neutron densities and radii are presented. A summary is given in Sec. VI. In Appendix A, supplemental figures are presented.

## II. CALCULATION OF $p$ SCATTERING

### A. Target densities

The theoretical densities of Pb isotopes, which are used as inputs for nucleon-nucleus folding potentials in  $\text{Pb}(p,p)$  calculations, are obtained via the RHB and SHFB calculations of spherical nuclei using the computational codes named DIRHB [26] and HFBRAD [29], respectively. For the former, the DD-ME2 [27] and DD-PC1 [28] interactions are used; in this paper, these are simply denoted by me2 and pc1, respectively. For the latter case, the SKM\* [30] and SLy4 [31] interactions are used. Note that the parameter sets of these structure models were adjusted to globally fit the binding energies and rms charge radii in wide mass-number regions that include  $^{40}\text{Ca}$  and  $^{208}\text{Pb}$ .

The experimental neutron densities of the Pb isotopes used in this paper are those of Refs. [5, 32], which were extracted by fitting the  $\text{Pb}(p,p)$  data at 295 MeV using the RIA calculation with the ddMH model, which was called medium-modified RIA calculation in the original paper. The neutron-density distribution is written in a sum-of-Gaussians (SOG) form and called the SOG-fit density in the present paper. The experimental proton densities are taken from Ref. [5]; they were obtained by unfolding the nuclear charge distribution determined by electric elastic scattering data [33].

Figures 1(a)-(c) show proton ( $\rho_p$ ) and neutron ( $\rho_n$ ) densities of  $^{204}\text{Pb}$ ,  $^{206}\text{Pb}$ , and  $^{208}\text{Pb}$ , and Fig. 1(d) shows  $4\pi r^2 \rho_p$  and  $4\pi r^2 \rho_n$  of  $^{208}\text{Pb}$ . The theoretical densities of the RHB (me2 and pc1) and SHFB (SKM\* and SLy4) calculations and the experimental SOG-fit density are shown. The proton scattering at  $E_p = 295$  MeV is a sensitive probe of the surface-neutron density around the peak position of  $4\pi r^2 \rho_n$  at  $r \sim 6$  fm, but it is insensitive

to the inner densities. Therefore, the SOG-fit neutron densities of Pb isotopes have large uncertainties in the  $r < 4$  fm region as shown by the error envelopes (filled area). Theoretical neutron densities depend upon structure models, but each model yields similar neutron densities between  $^{204}\text{Pb}$ ,  $^{206}\text{Pb}$ , and  $^{208}\text{Pb}$ . Comparing the theoretical model and SOG-fit neutron densities in the surface region, the me2 model shows the best agreement with the SOG-fit density, whereas other theoretical models show disagreements;  $4\pi r^2 \rho_n(r)$  obtained by the pc1, SKM\*, and SLy4 models exhibits a peak position that is slightly shifted outward compared with the SOG-fit and me2 densities. This peak-position shift causes deviation of the  $(p, p)$  cross sections from the data at backward angles, as discussed later in Sec. II B.

Figure 2(a) shows the theoretical and experimental values of  $r_p$  and  $r_n$ , whereas Fig. 2(b) shows the values of  $\Delta r_{np}$ . All theoretical models show smooth changes of  $r_p$  and  $r_n$  as the mass number  $A$  increases from  $^{204}\text{Pb}$  to  $^{208}\text{Pb}$ . The  $A$  dependence of  $r_p$  is quite similar between different models and is consistent with the experimental data. As for the neutron radii, the  $r_n$  and  $\Delta r_{np}$  change smoothly with the same slope as  $A$  increases in all theoretical models, meaning that the  $A$  dependence is approximately model independent though the absolute  $r_n$  values are model dependent. Compared with the smooth changes of the theoretical  $r_n$  and  $\Delta r_{np}$  values, the  $r_n$  values of the SOG-fit density seem to show a different  $A$  dependence—in particular, an enhancement of  $r_n$  and  $\Delta r_{np}$  at  $A = 208$  from  $^{206}\text{Pb}$  to  $^{208}\text{Pb}$ . However, this is not definite due to the large experimental errors that arise mainly from uncertainty in the internal neutron densities extracted from the  $(p, p)$  data.

## B. Reaction calculation of $p$ scattering at 295 MeV

Proton elastic scattering at  $E_p = 295$  MeV is calculated using RIA with the ddMH model (a modified MH model proposed by Sakaguchi *et al.* [19] by introducing density-dependent  $\sigma$ - and  $\omega$ -meson masses and coupling constants of the relativistic Love-Franey (RLF)  $NN$  interaction of the original MH model [16, 17]). The density dependence is considered as “medium effects” of the effective  $NN$  interaction, which includes various many-body effects in proton elastic scattering such as the Pauli blocking and multistep processes, in addition to the medium effects of meson properties. The RIA calculation with the ddMH model is performed in the default case, and that with the MH model is also performed in an optional case.

The parameter set of the density dependence used in this paper is the same as that used to analyze  $\text{Pb}(p, p)$  and  $\text{Ca}(p, p)$  at  $E_p = 295$  MeV in Refs. [5, 21]. This parameter set is the latest version calibrated to fit the updated data for  $p + ^{58}\text{Ni}$  at  $E_p = 295$  MeV and can well reproduce the  $^{40}\text{Ca}(p, p)$  data at  $E_p = 295$  MeV [21]. In the RIA framework with the MH and ddMH models,

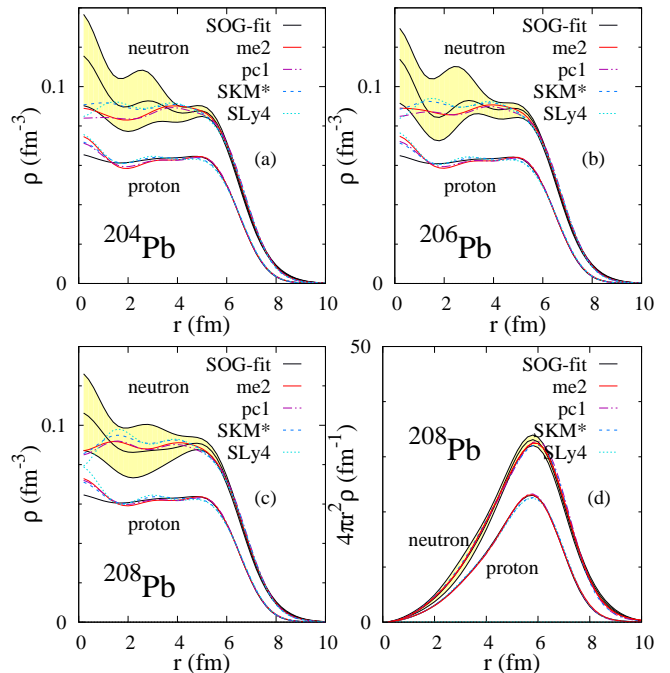


FIG. 1: Proton and neutron densities  $\rho_p(r)$  and  $\rho_n(r)$  for (a)  $^{204}\text{Pb}$ , (b)  $^{206}\text{Pb}$ , (c)  $^{208}\text{Pb}$ , and (d)  $4\pi r^2 \rho_n(r)$  of  $^{208}\text{Pb}$ . Theoretical densities are those of RHB (me2 and pc1) and SHFB (SKM\* and SLy4) calculations. The experimental SOG-fit densities are the neutron density (with error envelopes) extracted from the  $(p, p)$  data at  $E_p = 295$  MeV in Ref. [32] and the proton density of Ref. [5] obtained by unfolding the charge densities determined by electron scattering data [33]. In practice, the  $\rho_p(^{208}\text{Pb}; r)$  data are read from figures of Ref. [5], whereas  $\rho_n(^{204}\text{Pb}; r)$  and  $\rho_p(^{206}\text{Pb}; r)$  are constructed by  $r$  scaling of  $\rho_p(^{208}\text{Pb}; r)$  to adjust the point-proton radii.

the proton-nucleus potentials are calculated by folding the vector and scalar densities of target nuclei with the meson-exchange  $NN$  interaction. As the input target densities, the proton ( $\rho_p(r)$ ) and neutron ( $\rho_n(r)$ ) densities are used for the proton and neutron vector densities, whereas  $0.96\rho_p(r)$  and  $0.96\rho_n(r)$  are used for the proton and neutron scalar densities, respectively; this prescription of the scalar densities was adopted in Ref. [5] to fit the ddMH model to the  $^{58}\text{Ni}(p, p)$  data and applied to the  $\text{Pb}(p, p)$  analysis. Note that, in the RHB calculations, the scalar densities can be obtained without such an approximation, but give only a minor correction to the  $\text{Pb}(p, p)$  reactions at this energy. We adopt the prescription of the scalar densities for all models consistently with the calibration of the ddMH model.

The cross sections and analyzing powers of  $\text{Pb}(p, p)$  at 295 MeV obtained by the RIA calculation with the ddMH model are shown in Figs. 3 and 4, respectively, and the Rutherford ratio of the cross sections are shown in Fig. 5. In the results obtained using the pc1, SKM\*, and SLy4 densities, dip and peak positions in the diffraction pattern deviate from the experimental data, in particular, at

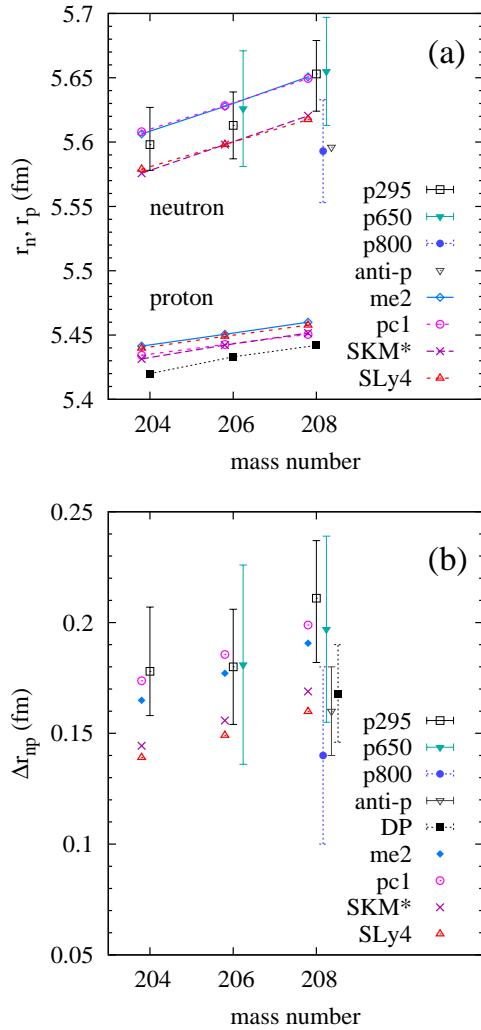


FIG. 2: (a) Rms point-proton and neutron radii and (b) neutron skin thickness of Pb isotopes. The theoretical values are those of RHB (me2 and pc1) and SHFB (SKM\* and SLy4) calculations. The experimental data are values of the SOG-fit density extracted from the  $(p, p)$  data at 295 MeV [5], those extracted from the  $(p, p)$  data at 800 MeV [13–15] and 650 MeV [4], and the  $x$ -ray cascade from antiprotonic atoms [6]. The experimental  $\Delta r_{np}$  value extracted from electric dipole polarization [10, 11] is also shown in (b).

backward angles, in which the dip (peak) positions shift to forward angles because of the slight outward shift of the  $4\pi r^2 \rho_n(r)$  peak position compared with the SOG-fit and me2 densities. The me2 result agrees better with the data than those of other theoretical densities, but a slight deviation from the data still remains. Therefore, the dip interval in the diffraction pattern is sensitive to the  $4\pi r^2 \rho_n(r)$  peak position, but does not necessarily correspond to the neutron radius  $r_n$ . For instance, the SKM\* density has a smaller value of  $r_n$  than the SOG-fit density, but it gives a shrunk diffraction pattern of the  $(p, p)$  cross sections consistent with the outward shift of the  $4\pi r^2 \rho_n(r)$  peak, indicating an expansion of the nu-

clear size probed by proton scattering.

To show reaction model dependence, the results obtained using the MH model with the SOG-fit and me2 densities are shown in Figs. 4 and 5 in comparison with the results of the ddMH model. The dip interval of the cross sections depends upon the effective  $NN$  interaction in the reaction model; compared with the ddMH results, the diffraction pattern of the MH model deviates forward, indicating that the range of the effective  $NN$  interaction in the MH model is slightly longer than that in the ddMH model.

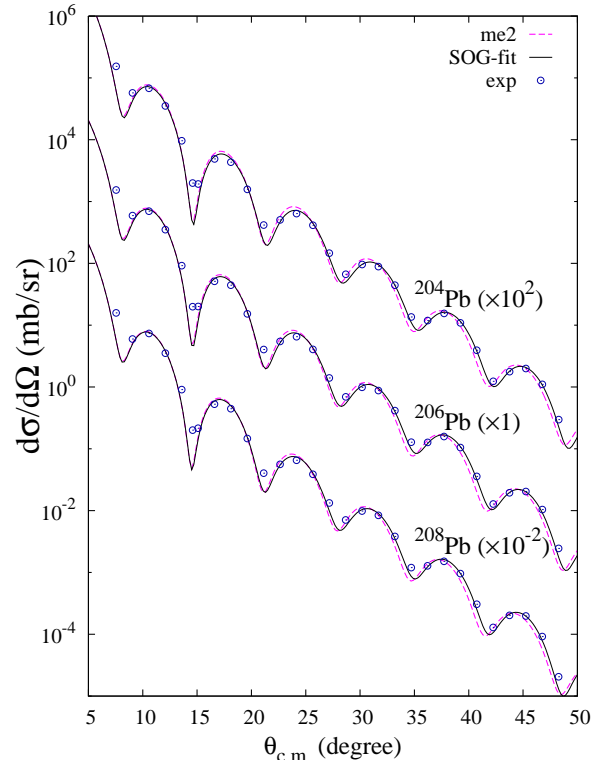


FIG. 3: Cross sections of Pb $(p, p)$  at 295 MeV obtained by RIA with the ddMH model using the SOG-fit and me2 densities together with the experimental data [5].

As shown in the results, the calculated  $(p, p)$  cross sections at 295 MeV are sensitive to differences between input neutron densities at the nuclear surface, and depend upon the effective  $NN$  interaction used in the nucleon-nucleus folding potential. However, in each model, the results for a series of isotopes from  $^{204}\text{Pb}$  to  $^{208}\text{Pb}$  are quite similar and deviation from the experimental data occurs systematically for the three isotopes. To see the isotopic similarities, the results of Pb isotopes are compared in Fig. 6 for densities and Fig. 7 for the Rutherford ratio of the cross sections on a linear scale. For each result of the SOG-fit, me2, pc1, SKM\*, SLy4, MH-SOG-fit, and MH-me2, the isotopic difference between  $^{204}\text{Pb}$ ,  $^{206}\text{Pb}$ , and  $^{208}\text{Pb}$  in the cross sections is small because surface densities in the  $r \gtrsim 6$  fm region of the three iso-

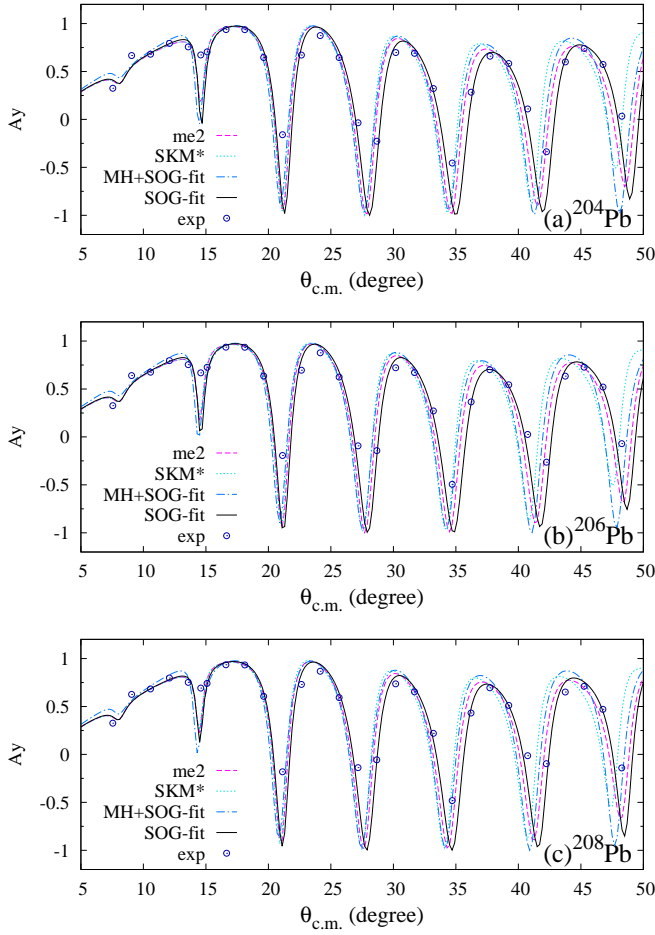


FIG. 4: Analyzing powers of  $Pb(p,p)$  at 295 MeV obtained by RIA with the ddMH model using the SOG-fit, me2, and SKM\* densities together with the experimental data from [5]. The result of the original MH model using the SOG-fit density is also shown for comparison.

topes approximately coincide, even in the linear plot of the Rutherford ratio (Fig. 7). These isotopic systematics are useful for a model-independent analysis of proton elastic scattering.

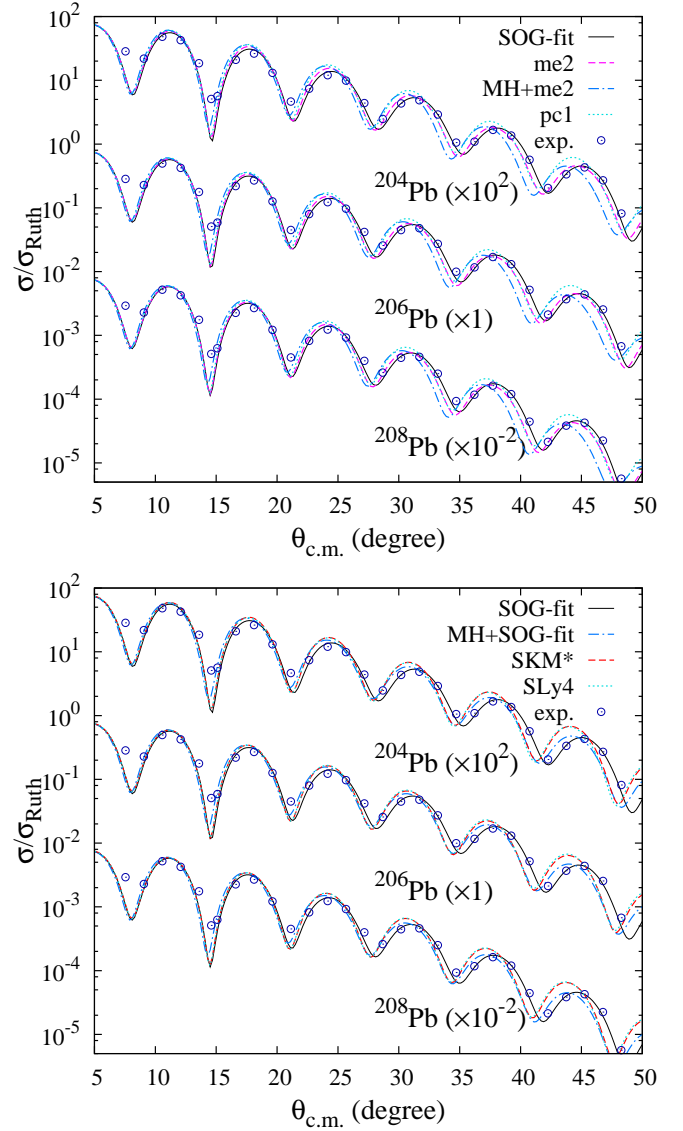


FIG. 5: Rutherford ratios of the  $Pb(p,p)$  cross sections at 295 MeV obtained with the ddMH model using the SOG-fit, me2, pc1, SKM, and SLy4 densities together with the experimental data from Ref. [5]. The results obtained using the original MH model using the SOG-fit (MH+SOG-fit) and me2 (MH+me2) densities are also shown for the purposes of comparison.

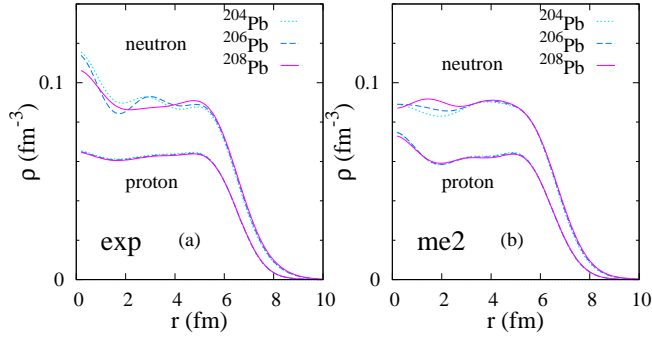


FIG. 6: (a) Experimental SOG-fit densities and (b) theoretical (me2) densities of the protons and neutrons of Pb isotopes.

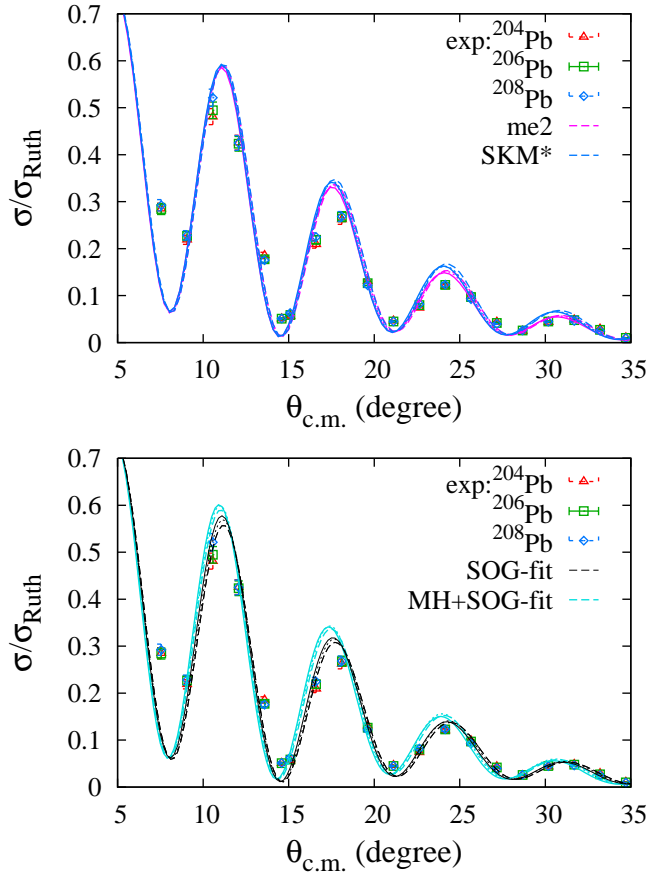


FIG. 7: Rutherford ratio of the  $(p, p)$  cross sections at 295 MeV, as obtained by RIA with the ddMH model using the SOG-fit, me2, and SKM\* densities together with the experimental data [5]. The results obtained using the original MH model using the SOG-fit (MH+SOG-fit) and me2 (MH+me2) densities are also shown. The calculated Rutherford ratios of the  $^{204}\text{Pb}(p, p)$ ,  $^{206}\text{Pb}(p, p)$ , and  $^{208}\text{Pb}(p, p)$  cross sections are plotted using dashed, dotted, and solid lines, respectively.

### III. ISOTOPIC ANALYSIS

#### A. Definitions of isotopic differences and ratios

By considering  $^{208}\text{Pb}$  as the reference nucleus, the isotopic density and radius differences and cross-section ratio are calculated for each model in the present isotopic analysis. The isotopic density and radius differences are respectively given as

$$D(\rho_{n,p}; r) \equiv \rho_{n,p}(^A\text{Pb}; r) - \rho_{n,p}(^{208}\text{Pb}; r), \quad (1)$$

$$\begin{aligned} D(r_{n,p}) &\equiv r_{n,p}(^A\text{Pb}) - r_{n,p}(^{208}\text{Pb}), \\ &= \frac{\int 4\pi r^4 D(\rho_{n,p}; r) dr}{A - 208} \end{aligned} \quad (2)$$

where  $\rho_{n(p)}(^A\text{Pb}; r)$  and  $r_{n(p)}(^A\text{Pb})$  are the neutron(proton) density and rms radius of  $^A\text{Pb}$ . The isotopic cross-section ratio is given as

$$R(\sigma; \theta_{c.m.}) \equiv \frac{d\sigma(^A\text{Pb})/d\Omega}{d\sigma(^{208}\text{Pb})/d\Omega}, \quad (3)$$

with differential cross sections in the center-of-mass frame. It is trivial that, even in the case of  $\rho_{p,n}(^A\text{Pb}; r) \propto \rho_{p,n}(^{208}\text{Pb}; r)$ ,  $R(\sigma; \theta)$  is not constant because of normalization of the target densities used for the folding potential and kinematical effects in the reaction.

Experimental values of  $R(\sigma; \theta_{c.m.})$  are obtained using the  $(p, p)$  cross section data at approximately the same angles in a series of Pb isotopes by omitting isotopic differences in the transformation from the laboratory frame to the center-of-mass frame, which is negligibly small in this mass-number region.

#### B. Isotopic difference of neutron radii and densities

The isotopic radius differences  $D(r_n)$  and  $D(r_p)$  are nothing but the relative radii of  $^A\text{Pb}$ , measured from  $^{208}\text{Pb}$ . The theoretical values of  $D(r_n)$  and  $D(r_p)$  are shown in Fig. 8 together with the experimental  $D(r_n)$  of the SOG-fit density and the  $D(r_p)$  values [5]. The theoretical results of RHB (me2 and pc1) and SHFB (SKM\* and SLy4) calculations are consistent and show linear dependences of  $D(r_n)$  and  $D(r_p)$  upon the neutron-number difference  $N - 126$  because of the isotopic systematics of  $r_n$  and  $r_p$  as discussed previously. The theoretical values of the isotopic proton radius difference,  $D(r_p) = -0.02$  fm for  $^{204}\text{Pb}$  and  $D(r_p) = -0.01$  fm for  $^{206}\text{Pb}$ , agree well with the experimental values reduced from the charge radii. For the isotopic neutron radius difference, the theoretical values are independent from structure models as  $D(^{204}\text{Pb}; r_n) \approx -0.04$  fm and  $D(^{206}\text{Pb}; r_n) \approx -0.02$  fm. They are contained in the experimental errors extracted from the  $(p, p)$  data at 295 MeV, but deviate from the experimental best-fit values  $D(r_n) = -0.055$  fm for  $^{204}\text{Pb}$  and  $D(r_n) = -0.040$  fm for  $^{206}\text{Pb}$  of the SOG-fit neutron density.

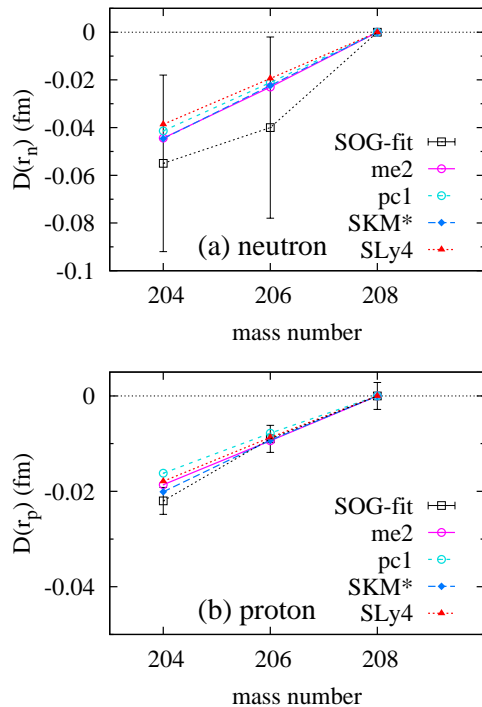


FIG. 8: Isotopic differences for (a) neutron and (b) proton radii,  $D(r_n)$  and  $D(r_p)$ , for the RHB (me2 and pc1) and SHFB (SKM\* and SLy4) calculations, and the experimental SOG-fit density.

The isotopic neutron-density differences in  $^{204}\text{Pb}$  and  $^{206}\text{Pb}$  of the SOG-fit, me2, and SKM\* densities are shown in Fig. 9. The one-neutron hole densities of the  $3p_{1/2}$  and  $2f_{5/2}$  orbits in  $^{208}\text{Pb}$  of the me2 density are shown for comparison. In the me2 and SKM\* densities,  $4\pi r^2 D(\rho_n)$  shows a remarkable reduction of the surface density in the  $6 \lesssim r \lesssim 8$  fm region from  $^{208}\text{Pb}$  to  $^{206}\text{Pb}$  because of the dominant  $(3p_{1/2})^{-2}$  and  $(3p_{3/2})^{-2}$  contributions, but contains the pairing effect and other higher-order effects beyond perturbation such as  $^{208}\text{Pb}$ -core shrinkage. Compared with the enhanced amplitude of  $4\pi r^2 D(\rho_n)$  at the surface, the amplitude in the internal region is relatively small and shows almost no specific character except for a small oscillation of the  $3p$ -hole component. The SOG-fit density shows a  $4\pi r^2 D(\rho_n)$  surface amplitude similar to the theoretical densities in the  $6 \lesssim r \lesssim 8$  fm region, but a strange behavior occurs in the  $2 \lesssim r \lesssim 4$  fm region—that is, a sharp peak with an opposite sign. Since the proton elastic scattering at 295 MeV is insensitive to this internal region, this sharp peak may be an artifact that accidentally occurred in the SOG fitting under the condition of total neutron-number conservation. However, this artifact in the internal region causes a sudden increase of  $r_n$  from  $^{206}\text{Pb}$  to  $^{208}\text{Pb}$  as understood by the relationship between  $D(\rho_n)$  and  $D(r_n)$  given in Eq. (2). Another difference between the SOG-fit and theoretical densities is seen in the  $4 \lesssim r \lesssim 6$  fm region.

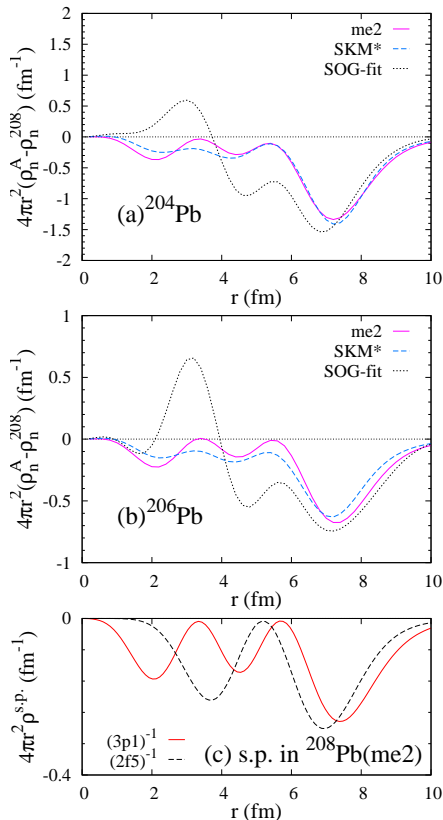


FIG. 9: Isotopic neutron-density differences ( $D(\rho_n)$ ) of (a)  $^{204}\text{Pb}$  and (b)  $^{206}\text{Pb}$  for the SOG-fit, me2, and SKM\* densities. (c) One-neutron hole densities ( $\rho^{s.p.}(r)$ ) of the  $3p_{1/2}$  and  $2f_{5/2}$  orbits in the  $^{208}\text{Pb}$  core obtained by the RHB (me2) calculation.  $4\pi r^2 D(\rho_n)$  and  $4\pi r^2 \rho^{s.p.}(r)$  are plotted as functions of  $r$ .

### C. Isotopic cross-section ratio

The isotopic cross-section ratios  $R(\sigma)$  of  $^{204}\text{Pb}$  and  $^{206}\text{Pb}$  to  $^{208}\text{Pb}$  are calculated by the ddMH model using the SOG-fit and theoretical densities. Figure 10 compares the results obtained using the SOG-fit, me2, and SKM\* densities, with the experimental values. The result calculated with the original MH model using the me2 density is also compared to see the dependence on the effective  $NN$  interaction in the reaction models. The isotopic cross-section ratio shows an oscillating behavior that reflects the diffraction pattern of the cross sections; the dip positions of  $R(\sigma)$  correspond to the dip angles of the  $^A\text{Pb}(p,p)$  cross sections, whereas the peak positions of  $R(\sigma)$  correspond to the dip angles of the  $^{208}\text{Pb}(p,p)$  cross sections. In principle, the oscillation amplitude of  $R(\sigma)$  is sensitive to the size difference between isotopes. The size shrinkage of  $^A\text{Pb}$  from  $^{208}\text{Pb}$  expands the diffraction pattern of  $\sigma(^A\text{Pb})$ , shifting the dip positions slightly to backward angles as compared with  $\sigma(^{208}\text{Pb})$ . This shift that originates in the nuclear size shrinkage increases the amplitude in one cycle of the oscillation of  $R(\sigma)$ . Com-

paring different model calculations the oscillation interval of  $R(\sigma)$  depends upon the structure and reaction models because of the model dependence of the dip positions of  $\sigma$  as shown in Fig. 5; however, the oscillation amplitude of  $R(\sigma)$  is similar between different models.

To see more details of the oscillation amplitude,  $R(\sigma)$  is plotted for yr rescaled angles  $\theta_{c.m.}^* = (\theta_{5th}^{SOG}/\theta_{5th}^{cal})\theta_{c.m.}$  so as to adjust the fifth peak angle ( $\theta_{5th}^{SOG}$ ) of the  $^{208}\text{Pb}(p,p)$  cross sections of SOG-fit with that ( $\theta_{5th}^{theor}$ ) of the other calculations. The  $\theta_{c.m.}^*$ -plots of  $R(\sigma)$  for  $^{204}\text{Pb}$  and  $^{206}\text{Pb}$  are shown in Figs. 10(c) and (d), respectively. After rescaling the angles, the model dependence of  $R(\sigma)$  becomes small except for the  $\theta^* > 42^\circ$  region as expected from that the isotopic neutron-density differences  $D(\rho_n)$  in the surface region being similar between various theoretical densities and the SOG-fit density. This result indicates that a model-independent discussion is possible in isotopic analysis using the rescaled angles  $\theta^*$ .

Compared with the experimental  $R(\sigma)$  obtained from the  $(p,p)$  cross section data, the  $R(\sigma)$ s calculated using the theoretical and SOG-fit densities slightly overshoot the experimental oscillation amplitude for  $^{204}\text{Pb}$  and  $^{206}\text{Pb}$  as shown by the  $\theta^*$ -plots in Figs. 10(c) and (d), respectively.

## IV. HOLE-MODEL ANALYSIS

### A. Model of the $^{208}\text{Pb}$ core with holes

As discussed previously, isotopic similarities are found in the neutron density and  $(p,p)$  cross sections in a series of Pb isotopes, indicating that isotopic differences can be described by a perturbative treatment based on the  $^{208}\text{Pb}$  core. By assuming a  $^{208}\text{Pb}$  core and hole contributions, I introduce a model (called the hole model in this paper) for the neutron densities of  $^{204}\text{Pb}$  and  $^{206}\text{Pb}$  and discuss the connection between  $D(\rho_n)$  and  $R(\sigma)$ .

The hole-model neutron densities of  $^{204}\text{Pb}$  and  $^{206}\text{Pb}$  are expressed using two parameters for the neutron-hole contribution and size scaling of the  $^{208}\text{Pb}$ -core as

$$\rho_n(^A\text{Pb}; r) = \mathcal{N}_0 \left\{ \rho_n(^{208}\text{Pb}; r/s) - h \rho_{3p_{1/2}}^{s.p.}(r/s) \right\}, \quad (4)$$

$$\mathcal{N}_0 = \frac{N}{126 - h s^3}, \quad (5)$$

$$\delta_s \equiv s - 1 \quad (6)$$

where  $\mathcal{N}_0$  is the normalization factor for the total neutron number,  $\rho_{3p_{1/2}}^{s.p.}$  is the neutron single-particle density of the  $3p_{1/2}$  orbit in the  $^{208}\text{Pb}$ -core,  $s$  is the  $r$ -scaling factor of the core-size shrinkage, which is given by the scaling parameter  $\delta_s$ , and  $h$  is a model parameter for the  $3p_{1/2}$ -hole contribution. Note that  $h$  does not necessarily equal the actual neutron  $3p_{1/2}$ -hole number but is a parameter of the effective hole number for the  $3p_{1/2}$ -orbit contribution to neutron density. For the no-scaling ( $\delta = 0$ )



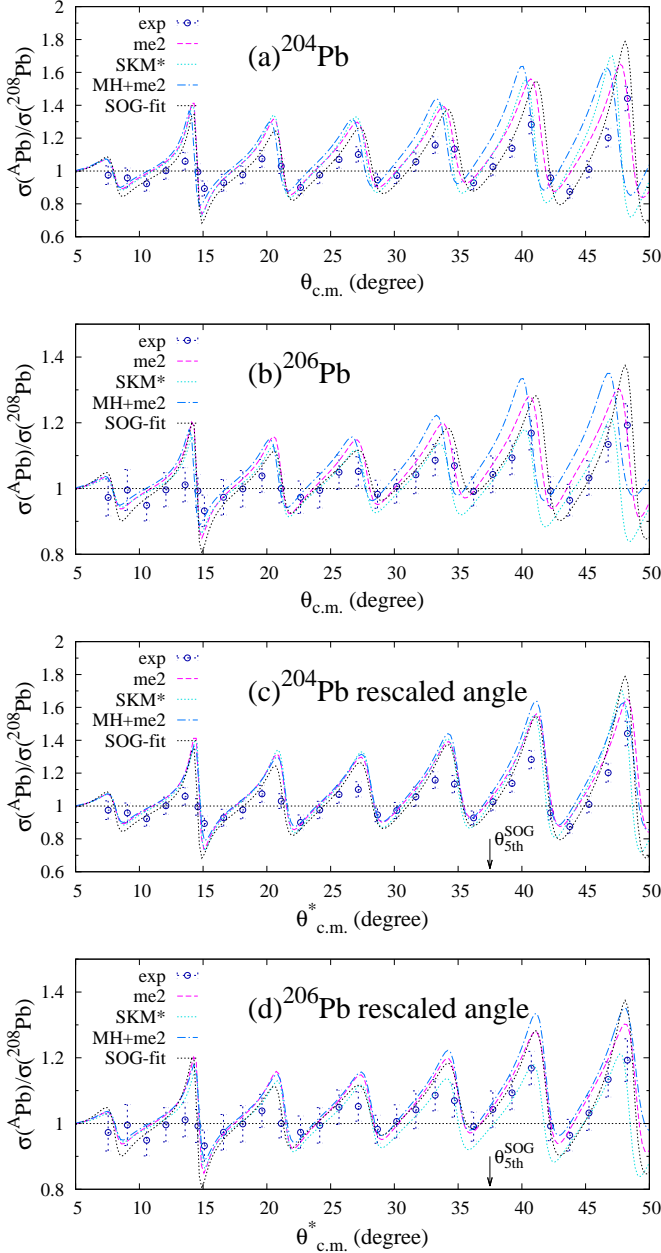


FIG. 10: Isotopic cross-section ratios  $R(\sigma)$  of (a)  $^{204}\text{Pb}(p,p)$  and (b)  $^{206}\text{Pb}(p,p)$  to  $^{208}\text{Pb}(p,p)$  at 295 MeV obtained with the ddMH model using the SOG-fit, me2, and SKM\* densities plotted as functions of  $\theta_{\text{c.m.}}$  together with the experimental values obtained from the  $(p,p)$  cross section data [5]. The result obtained using the original MH model using the me2 (MH+me2) density is also shown. The  $\theta_{\text{c.m.}}$ -plots of  $R(\sigma)$  for (c)  $^{204}\text{Pb}$  and (d)  $^{206}\text{Pb}$  for the rescaled angles  $\theta_{\text{c.m.}}^* = (\theta_{5\text{th}}^{\text{SOG}}/\theta_{5\text{th}}^{\text{cal}})\theta_{\text{c.m.}}$  adjusted to fit the fifth peak angles ( $\theta_{5\text{th}}^{\text{theor}}$ ) of the  $^{208}\text{Pb}(p,p)$  cross sections of theoretical results to that ( $\theta_{5\text{th}}^{\text{SOG}}$ ) of the SOG-fit result. The fitting angle  $\theta_{5\text{th}}^{\text{SOG}}$  is indicated using arrows.

case, the hole model neutron density  $\rho_n(^A\text{Pb}; r)$  is ap-

proximately written as

$$\rho_n(^A\text{Pb}; r) \approx \rho_n(^{208}\text{Pb}; r) - h\rho_{3p_{1/2}}^{\text{s.p.}}(r) - (126 - N - h)\frac{\rho_n(^{208}\text{Pb}; r)}{126}, \quad (7)$$

meaning that the total hole contribution is approximated by the  $3p_{1/2}$ -hole contribution and an overall reduction in the total neutron density, which contains contributions from other orbits. With this expression of two parameters,  $h$  for the effective  $3p_{1/2}$ -hole number and  $\delta_s$  for the size shrinkage, the hole model can simulate the densities of various configurations such as the  $(2f_{5/2})^{-h}$  configuration and also describe “equivalent” neutron densities to other theoretical densities that reproduce  $R(\sigma)$ . Examples of the hole model neutron densities equivalent to the  $(2f_{5/2})^{-h}$  configuration and the me2 density are demonstrated in Appendix A.

In the present hole-model analysis, the hole-model density is used only for the neutron densities of  $^{204}\text{Pb}$  and  $^{206}\text{Pb}$  but the proton part is unchanged from the original proton densities of  $^{204}\text{Pb}$  and  $^{206}\text{Pb}$ . For the parameter  $h$  of the effective  $3p_{1/2}$ -hole number, the hole-model densities with  $h = 0, 0.5, \dots, 2$  are used and labeled as  $(0h, \delta_s), (0.5h, \delta_s), \dots, (2h, \delta_s)$ , respectively.

I first perform isotopic analysis using the hole model with the  $^{208}\text{Pb}$ -core and  $3p_{1/2}$ -orbit densities obtained by the me2 calculation to clarify the correspondence of  $R(\sigma)$  to  $D(\rho_n)$  and  $D(r_n)$ . Then, I perform the hole-model analysis using the SOG-fit  $^{208}\text{Pb}$ -core and the me2  $3p_{1/2}$ -orbit densities to obtain optimized parameter sets  $h$  and  $\delta_s$  of the hole model by fitting the experimental  $R(\sigma)$  obtained by the  $\text{Pb}(p,p)$  cross section data at 295 MeV.

## B. Hole-model analysis with the me2-core density

The isotopic neutron-density difference  $D(\rho_n)$  and the isotopic cross-section ratio  $R(\sigma)$  for  $^{206}\text{Pb}$  obtained using the hole-model density with the me2-core are shown in Fig. 11. The 0h, 1h, and 2h results corresponding to the  $3p_{1/2}$ -hole numbers  $h = 0, 1, \text{ and } 2$  in the range of  $-0.2\% < \delta_s < 0$  (0.2–0% core shrinkage) are illustrated by the yellow, pink, and blue-colored areas, respectively. The oscillation amplitude of  $R(\sigma)$  depends upon the size-scaling parameter  $\delta_s$ ; it becomes larger as  $^{206}\text{Pb}$  size shrinks from the  $^{208}\text{Pb}$  core. The increase of  $h$  (the effective  $3p_{1/2}$ -hole number) changes the surface behavior of  $D(\rho_n)$ ; it reduces and enhances the surface amplitude of  $4\pi r^2 D(\rho_n)$  in the  $r \lesssim 7$  fm and  $7 \lesssim r \lesssim \rho_{3p_{1/2}}^{\text{s.p.}}$  (Fig. 9(c)). This change in  $4\pi r^2 D(\rho_n)$  increases  $R(\sigma)$ .

Let me now discuss each effect of the size scaling and increase of  $h$  upon  $R(\sigma)$  via changes in  $D(\rho_n)$  and  $D(r_n)$  in greater detail. First, I shall discuss the size-scaling effect by changing only  $\delta_s$  of the 0h (no-hole) case of  $^{206}\text{Pb}$ . The results are shown in Figs. 12 and 13. Figures 12(a),

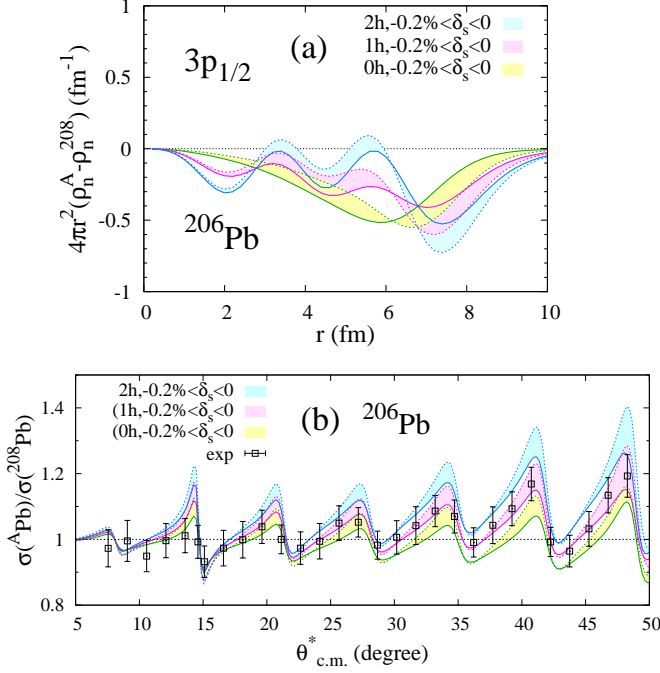


FIG. 11: (a) Isotopic neutron-density difference  $D(\rho_n)$  and (b) isotopic cross-section ratio  $R(\sigma)$  for  $^{206}\text{Pb}$  obtained using the hole model (me2-core) with  $(0h, -0.2\% \leq \delta_s \leq 0\%)$ ,  $(1h, -0.2\% \leq \delta_s \leq 0\%)$ , and  $(2h, -0.2\% \leq \delta_s \leq 0\%)$ , as shown by the color-filled areas surrounded by solid and dotted lines for  $\delta_s = 0\%$  and  $\delta_s = -0.2\%$ , respectively. The calculated  $R(\sigma)$  is plotted for rescaled angles  $\theta_{\text{c.m.}}^*$ . The experimental values obtained from the  $(p, p)$  data [5] are also shown.

(b), and (c) show  $4\pi r^2 D(\rho_n)$ ,  $\rho_n(r)$ , and  $4\pi r^2 \rho_n(r)$  for  $-1\% \leq \delta_s \leq 0\%$ , respectively. Figures 13(a) and (b) show the results of  $\sigma$  and  $R(\sigma)$ , respectively. For a clear visualization,  $\rho_n(r)$  and  $4\pi r^2 \rho_n(r)$  in an extreme case of  $\delta_s = -3\%$  are shown in Figs. 12(d) and (e), respectively. As the size shrinks from  $\delta_s = 0\%$  to  $-1\%$ ,  $\rho_n(r)$  increases in the  $r < 6$  fm region and decreases in the  $r > 6$  fm region (Figs. 12(b) and (d)); therefore, the peak position of  $4\pi r^2 \rho_n(r)$  shifts inwardly (Figs. 12(c) and (e)). The inward shift of the  $4\pi r^2 \rho_n(r)$  peak causes an outward shift of the diffraction pattern of the cross section (Fig. 13(a)) and enhances the oscillation amplitude of  $R(\sigma)$ , which monotonically increases as  $\delta_s$  decreases (Fig. 13(b)). This indicates that the oscillation amplitude of  $R(\sigma)$  is a sensitive measure of the shrinkage of  $^{206}\text{Pb}$  relative to  $^{208}\text{Pb}$ .

Next, I discuss the  $3p_{1/2}$ -hole contribution effects, which provide a nontrivial change of the density shape in the surface region. The density and cross sections obtained for the two-hole (2h) case are compared with those for the no-hole case in Figs. 12 and 15, respectively; to eliminate the size changing effect, I choose  $\delta_s$  independently for the 0h and 2h cases so that approximately the same  $D(r_n)$  values will be given in the two cases as  $D(r_n) \approx -0.024$  fm for  $^{206}\text{Pb}$  and  $D(r_n) \approx -0.046$  fm for  $^{204}\text{Pb}$ . The densities of  $^{206}\text{Pb}$  are shown in Fig. 12,

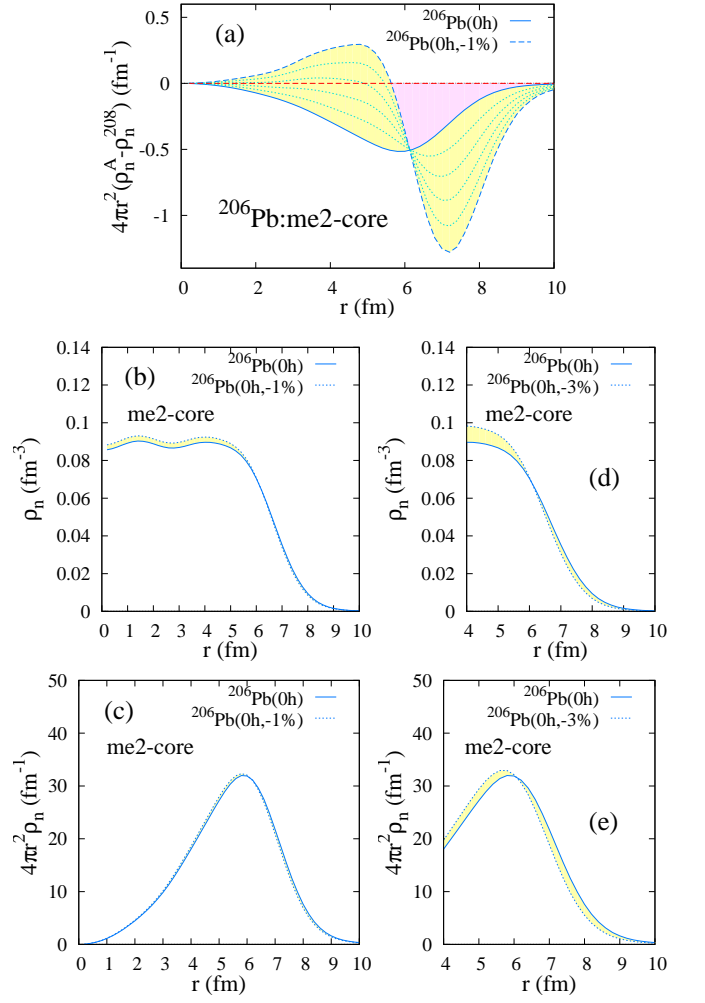


FIG. 12:  $\delta_s$  (size scaling) dependence of the hole-model neutron density of  $^{206}\text{Pb}$  with the me2-core in the zero hole case,  $(0h, \delta_s)$ . (a) Isotopic neutron-density difference  $D(\rho_n)$  for  $\delta_s = \{-1\%, -0.8\%, \dots, -0.2\%, 0\%\}$ . (b)  $\rho_n(r)$  and (c)  $4\pi r^2 \rho_n(r)$  for  $\delta_s = -1\%$  and (d)  $\rho_n(r)$  and (e)  $4\pi r^2 \rho_n(r)$  for  $\delta_s = -3\%$ , as compared with the  $\delta_s = 0\%$  (no scaling) case.

the results of the  $^{206}\text{Pb}(p, p)$  cross sections are shown in Figs. 12(a) and (b), and those for  $^{204}\text{Pb}(p, p)$  cross sections are presented in Fig. 15(c). Figures 12(d) and (e) display  $\rho_n(^{208}\text{Pb}) - 10 \times D(\rho_n)$  with 10 times enhanced  $D(\rho_n)$  to show the difference between the 0h and 2h densities more clearly. The dominant effect of the  $3p_{1/2}$ -hole contribution is an enhancement of the surface density in the  $5 \text{ fm} < r < 7 \text{ fm}$  region around the peak position of  $4\pi r^2 \rho_n(r)$ , whereas the contribution to the tail density in the  $r > 7 \text{ fm}$  region is relatively small (Fig. 12 (a),(c), and (e)). This density change by the  $3p_{1/2}$ -hole contribution globally raises the cross sections of  $^{206}\text{Pb}$  (Fig. 15(a)); therefore, it causes an upward shift of the isotopic cross-section ratio  $R(\sigma)$  without changing its angular dependence (Fig. 15(b)). Note that, the parallel shift of  $R(\sigma)$  with increasing  $h$  is obtained only when

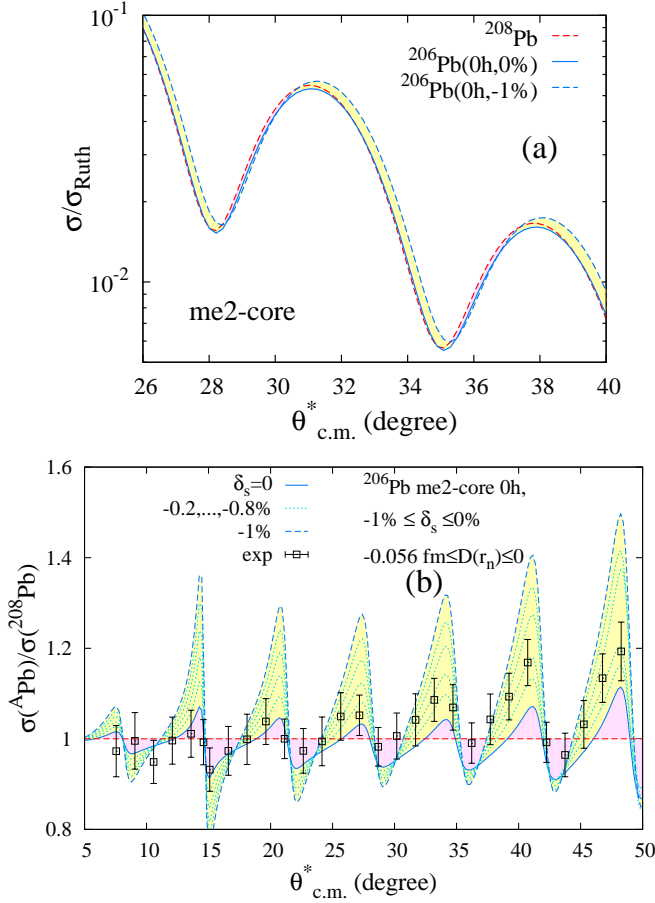


FIG. 13:  $\delta_s$  (size scaling) dependence of the cross sections and isotopic cross-section ratio for  $^{206}\text{Pb}(p,p)$  at 295 MeV, as obtained using the hole model (me2-core) in the zero hole case,  $(0h, \delta_s)$ . (a) Rutherford ratio of the  $^{206}\text{Pb}(p,p)$  cross sections for  $\delta_s = 0\%$  and  $\delta_s = -1\%$  compared with that of  $^{208}\text{Pb}(p,p)$ . (b) Isotopic cross-section ratio  $R(\sigma)$  of  $^{206}\text{Pb}$  to  $^{208}\text{Pb}$ , as obtained using the  $(0h, \delta_s)$  densities with  $\delta_s = \{-1\%, -0.8\%, \dots, -0.2\%, 0\%\}$ , which give  $D(r_n) = \{-0.56 \text{ fm}, -0.45 \text{ fm}, \dots, -0.11 \text{ fm}, 0 \text{ fm}\}$ . The calculated  $R(\sigma)$  is plotted for rescaled angles  $\theta_{\text{c.m.}}^*$ . The experimental values obtained from the  $(p,p)$  data [5] are also shown.

$D(r_n)$  is kept constant. The same analysis is performed for  $^{204}\text{Pb}$ , and a qualitatively consistent result is obtained (Fig. 15(c)).

In Figs. 15 (b) and (c), the  $R(\sigma)$  obtained using the hole-model density is compared with that obtained using the me2 and SKM\* densities. The me2(SK M\*) density gives  $D(r_n) = -0.023 \text{ fm}$  ( $-0.022 \text{ fm}$ ) for  $^{206}\text{Pb}$  and  $-0.044 \text{ fm}$  ( $-0.045 \text{ fm}$ ) for  $^{204}\text{Pb}$ , which are consistent with the  $D(r_n)$  values of the hole-model density presented herein. The oscillation amplitude of  $R(\sigma)$  is almost consistent between the hole-model, me2, and SKM\* densities, meaning that it is determined by  $D(r_n)$  independently from details of model densities.

The present analyses of  $\delta_s$  and  $h$  dependences indicate

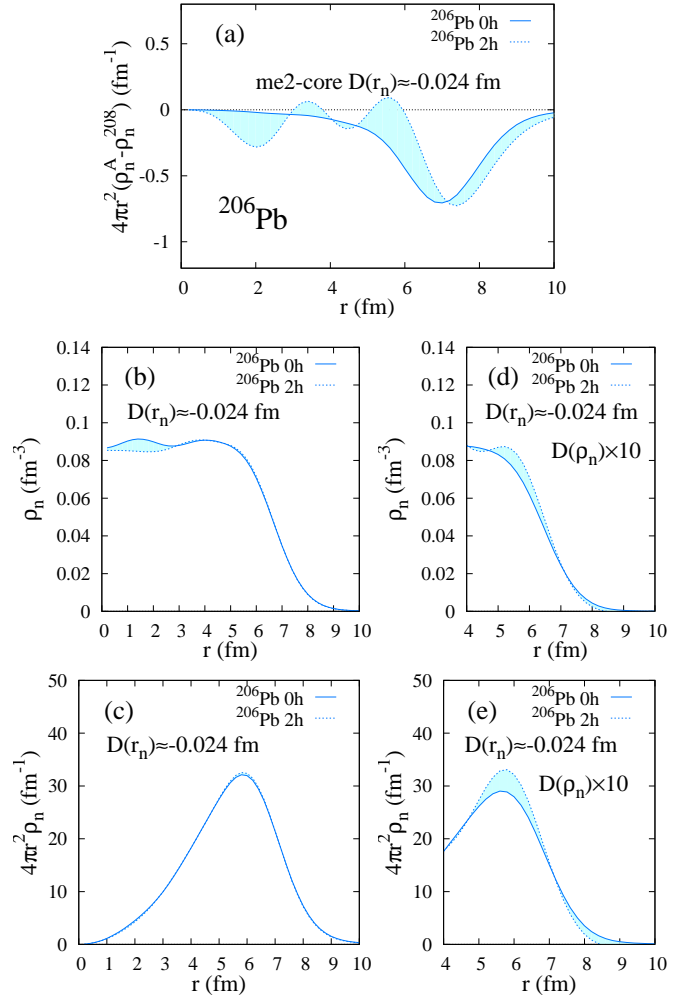


FIG. 14: Neutron densities of  $^{206}\text{Pb}$  for the hole model (me2-core) with  $(0h, \delta_s = -0.4\%)$  and  $(2h, \delta_s = -0.2\%)$  yielding  $D(r_n) = -0.023 \text{ fm}$  and  $-0.025 \text{ fm}$ , respectively. (a) Isotopic neutron-density difference  $4\pi r^2 D(\rho_n)$  and neutron densities (b)  $\rho_n(r)$  and (c)  $4\pi r^2 \rho_n(r)$ . To see the difference between the 0h and 2h densities more clearly,  $\rho_n(^{208}\text{Pb}) - 10D(\rho_n)$  with 10 times enhanced  $D(\rho_n)$  is displayed in (d), and the  $4\pi r^2$ -weighted version is displayed in (e).

the clear correspondence of  $R(\sigma)$  to  $D(\rho_n)$  and  $D(r_n)$ . Namely, the oscillation amplitude of  $R(\sigma)$  is a good measure to determine the isotopic neutron radius difference  $D(r_n)$ , whereas deviation of the center value of the oscillation from  $R = 1$  is a sensitive probe to the surface shape of the isotopic neutron-density difference  $D(\rho_n)$ .

### C. Hole-model analysis with the experimental SOG-fit core density

Using the SOG-fit core density, the hole-model analysis is performed in a similar way to Sec. IV B for the me2-core density, and qualitatively consistent results are obtained. The  $R(\sigma)$  result obtained by the RIA+ddMH

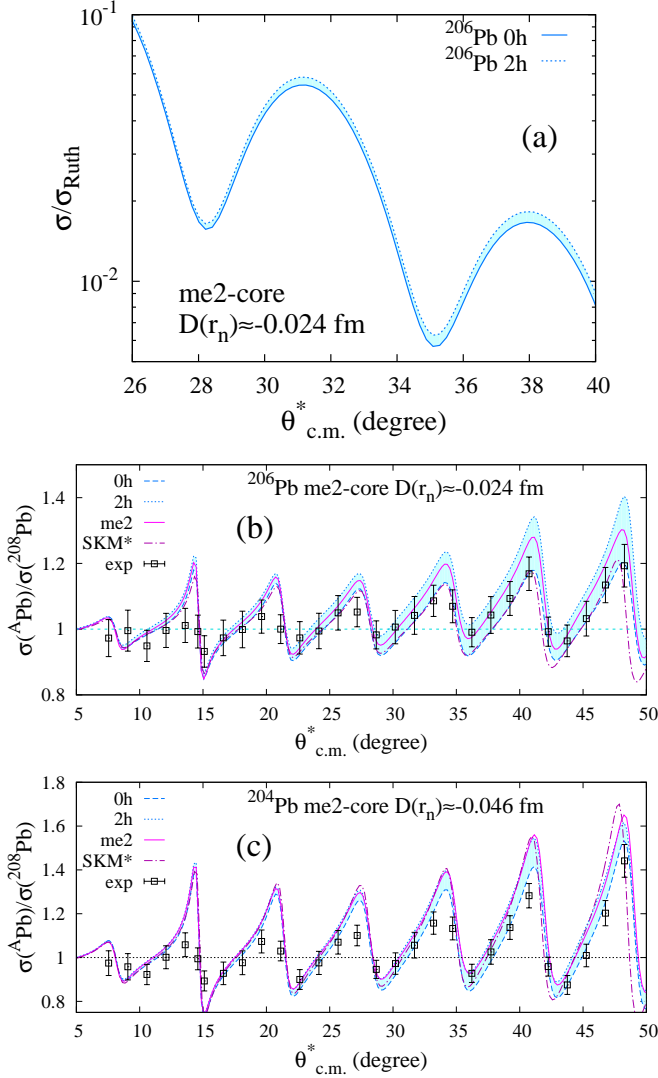


FIG. 15: (a) Rutherford ratio and (b) isotopic cross-section ratio  $R(\sigma)$  for  $^{206}\text{Pb}(p,p)$  at 295 MeV obtained using the hole model (me2-core) with  $(0h, \delta_s = -0.4\%)$  and  $(2h, \delta_s = -0.2\%)$ , which respectively give  $D(r_n) = -0.023$  fm and  $-0.025$  fm. (c)  $R(\sigma)$  for  $^{204}\text{Pb}$  obtained using the  $(0h, \delta_s = -0.8\%)$  density with  $D(r_n) = -0.045$  fm and the  $(2h, \delta_s = -0.6\%)$  density with  $D(r_n) = -0.047$  fm. Theoretical  $R(\sigma)$  values obtained using the me2 and SKM\* densities and experimental values obtained from the  $(p,p)$  data [5] are also shown in (b) and (c). The calculated results are plotted for rescaled angles  $\theta_{\text{c.m.}}^*$ .

calculation with the hole-model (SOG-core) density is shown in Fig. 16. Figures 16(a) and (b) show the  $\delta_s$  and  $h$  dependences of  $R(\sigma)$  for  $^{206}\text{Pb}$ , and Figs. 16(c) and (d) show the results for  $^{204}\text{Pb}$ . For  $^{206}\text{Pb}$ , the hole-model density with  $(0h, -0.7\%)$  (which has  $D(r_n) = -0.040$  fm, same as the SOG-fit density) overshoots the oscillation amplitude of the experimental  $R(\sigma)$  (see the red line in Fig. 16(a)). This indicates that the value  $D(r_n) = -0.040$  fm of the SOG-fit density for  $^{206}\text{Pb}$  may

be too large; similarly, the hole-model density of  $^{204}\text{Pb}$  with  $(0h, -1\%)$  has  $D(r_n) = -0.057$  fm, which is almost the same as the SOG-fit density, but seems to overshoot the oscillation amplitude of the experimental  $R(\sigma)$  (see the red line in Fig. 16(c)), meaning that the value of  $D(r_n) = -0.057$  fm for  $^{204}\text{Pb}$  is unlikely.

The optimal parameter set of  $h$  and  $\delta_s$  is sought for the hole model to fit the experimental  $R(\sigma)$ . First, I choose the favored parameter sets among the 0h densities,  $(0h, -0.2\%)$  with  $D(r_n) = -0.011$  fm for  $^{206}\text{Pb}$  and  $(0h, -0.4\%)$  with  $D(r_n) = -0.023$  fm for  $^{204}\text{Pb}$ , to reproduce the slope in one cycle of the oscillation amplitude of the experimental  $R(\sigma)$ ; then, I change the effective hole number  $h$ , maintaining the optimal  $D(r_n)$  values. The calculated  $R(\sigma)$  obtained using the 0h, 1h, and 2h densities with  $D(r_n) \approx -0.01$  fm ( $-0.02$  fm) for  $^{206}\text{Pb}$  ( $^{204}\text{Pb}$ ) is shown in Fig. 16(b) (Fig. 16(d)). Finally, the  $(1h, -0.01\%)$  density with  $D(r_n) = -0.012$  fm is obtained as an optimized solution for  $^{206}\text{Pb}$ , which describes the experimental  $R(\sigma)$ , and an optimized set  $(1h, -0.03\%)$  with  $D(r_n) = -0.023$  fm is obtained for  $^{204}\text{Pb}$ . The  $R(\sigma)$  values calculated using the optimized solutions are shown by solid lines in Figs. 16 (b) and (d).

#### D. Uncertainty in $D(r_n)$

To discuss the uncertainty in determining  $D(r_n)$  from the experimental  $R(\sigma)$ , I calculate the  $\chi^2$  values of  $R(\sigma)$  for the hole model. In the present analysis of  $R(\sigma)$ , the angular resolution of the experimental  $(p,p)$  cross section data is not taken into account, but it can have crucial effects at the forward and dip angles of the cross sections. Therefore,  $\chi^2$  is calculated using a total of 17 datapoints in a “safe” region by eliminating seven datapoints at the forward angles and five at the dip angles. In Fig. 17, the  $\chi^2$  values obtained for  $h = \{0, 0.5, \dots, 2\}$  and  $\delta_s = \{0\%, 0.1\%, \dots, 1.0\%\}$  are plotted as functions of  $D(r_n)$ .

The results for  $^{204}\text{Pb}$  and  $^{206}\text{Pb}$  of the hole model with the SOG-fit core are shown in Figs. 17(a) and (b). The absolute values of the calculated  $\chi^2$  are meaningless because the experimental errors of  $R(\sigma)$  are estimated by assuming independent errors of the  $^A\text{Pb}$  and  $^{208}\text{Pb}$  cross sections though the  $A$ -independent systematic errors should be removed. To roughly estimate the uncertainty, I here adopt a criterion for the acceptable  $\chi^2$  range as less than three times the minimum value  $\chi_{\text{min}}^2$  as  $\chi^2 \lesssim 3\chi_{\text{min}}^2$ . From the acceptable ranges of this criterion, which are shown by dotted lines in the figures,  $D(r_n) = -0.03$ – $-0.006$  fm for  $^{206}\text{Pb}$  and  $D(r_n) = -0.05$ – $-0.006$  fm for  $^{204}\text{Pb}$  are obtained. The  $\chi^2$  values for the SOG-fit density are  $\chi^2 = 14$  for  $^{206}\text{Pb}$  and  $\chi^2 = 52$  for  $^{204}\text{Pb}$ , which exceed the acceptable range because the systematics between the Pb isotopes was not taken into account in the fitting of Ref. [5].

For the hole model with the me2 core, the  $\chi^2$  values are calculated using rescaled angles  $\theta^*$ , and the results obtained for  $^{204}\text{Pb}$  and  $^{206}\text{Pb}$  are shown in Figs. 17(c) and

(d), respectively. The results of the me2 core are almost consistent with those of the SOG-fit core meaning that the present hole-model analysis of  $R(\sigma)$  can obtain  $D(r_n)$  values almost independently from the adopted  $^{208}\text{Pb}$ -core density. In Table I, the values of  $D(r_n)$  and  $\chi^2$  obtained by the hole models (SOG-fit and me2  $^{208}\text{Pb}$  cores) are summarized in comparison with those of the SOG-fit and me2 densities of the Pb isotopes.

TABLE I:  $\chi^2$  values of  $R(\sigma)$  for the SOG-fit, me2, hole model (SOG-core), and hole model (me2-core) densities.  $D(r_n)$  values are also listed. For the hole models, the  $\chi^2$  and  $D(r_n)$  values for the optimized parameter sets are listed together with the acceptable ranges estimated by  $\chi^2$  values.

	$^{204}\text{Pb}$		$^{206}\text{Pb}$	
	$D(r_n)$ (fm)	$\chi^2$	$D(r_n)$ (fm)	$\chi^2$
SOG-fit	-0.055	52	-0.040	14
me2	-0.044	52	-0.023	14
hole model (optimized)	$D(r_n)$ (fm)	$\chi^2_{\min}$	$D(r_n)$ (fm)	$\chi^2_{\min}$
SOG-core	-0.023	1.2	-0.012	3.9
me2-core	-0.024	1.9	-0.012	3.6
(acceptable)	-0.05 $\sim$ -0.006		-0.03 $\sim$ -0.006	

## V. IMPROVED NEUTRON DENSITIES AND RADII OF PB ISOTOPES

### A. Reconstruction of neutron densities

As mentioned previously, the SOG-fit density overshoots the oscillation amplitude of the experimental  $R(\sigma)$ . The reason for this failure in reproducing  $R(\sigma)$  is that the fitting was performed independently for each isotope without taking the isotopic systematics into account. From the SOG-fit density, I reconstruct the improved neutron densities of Pb isotopes that can describe experimental  $R(\sigma)$  as follows. First, the neutron density of  $^{206}\text{Pb}$  is obtained by averaging three densities of  $^{206}\text{Pb}$ ,  $^{206}\text{Pb}$ , and  $^{206}\text{Pb}$  given by the SOG-fit density to avoid a risk from uncertainty of the SOG-fit density in the internal region. Next, the neutron densities of  $^{208}\text{Pb}$  and  $^{204}\text{Pb}$  are constructed to reproduce the  $D(\rho_n)$  of the best solution of the hole model. The density of the Pb isotopes obtained with these procedures is called the ‘‘averaged-model’’ density. In Fig. 18, the averaged-model density is shown in comparison with the SOG-fit and me2 densities. The averaged-model density is similar to the SOG-fit density. The  $D(\rho_n)$ s of the averaged model, SOG-fit, and me2 densities are compared in Fig. 19. Note that the  $D(\rho_n)$  of the averaged model is tuned to fit the  $R(\sigma)$  data in the hole-model analysis. The surface peak shape

of  $4\pi r^2 D(\rho_n)$  in the 6 fm  $\lesssim r \lesssim$  8 fm region is similar between three kinds of densities; however, a difference is found in the internal  $r \lesssim$  5 fm region, to which  $(p, p)$  at 295 MeV is insensitive. The flopping behavior of  $4\pi r^2 D(\rho_n)$  found in the SOG-fit density disappears in the averaged-model density, which shows a smooth behavior in the internal region similar to theoretical densities such as the SKM\* density, rather than the SOG-fit density.

$\text{Pb}(p, p)$  at 295 MeV is calculated using RIA+ddMH with the averaged-model density. The results of  $R(\sigma)$ ,  $\sigma$ , and  $A_y$  are shown in Figs. 22, 20, and 21, respectively, and compared with those obtained with the SOG-fit and me2 densities.  $R(\sigma)$  is significantly improved by the averaged-model density compared with other densities because  $D(\rho_n)$  is tuned to fit the  $R(\sigma)$  data. Moreover, the averaged-model density successfully describes the cross sections and analyzing powers in a quality almost equivalent to the SOG-fit density.

In Fig. 23, the neutron radius ( $r_n$ ) and skin thickness ( $\Delta r_{np}$ ) obtained by the present averaged model are shown in comparison with the experimental and theoretical values. The averaged model yields smooth changes of  $r_n$  and  $\Delta r_{np}$  in a series of Pb isotopes from  $^{204}\text{Pb}$  to  $^{208}\text{Pb}$ . The values are within the experimental errors of the SOG fitting extracted from the  $(p, p)$  data at 295 MeV. It is difficult to quantitatively discuss the systematic errors of the present result because the angular resolutions and systematic errors of the experimental data are not taken into account in the present analysis. In Fig. 23, I present a rough estimation of the error range of  $r_n$  for  $^{208}\text{Pb}$  using the acceptable range  $D(r_n) = -0.03 \sim -0.006$  fm obtained by hole-model analysis and the  $r_n$  value of  $^{206}\text{Pb}$  of the averaged model.

## VI. SUMMARY

A new method of reaction analysis for proton elastic scattering was proposed by combining systematic analyses of nuclear structure and reaction in a series of isotopes. This method was applied to  $^{204}\text{Pb}(p, p)$ ,  $^{206}\text{Pb}(p, p)$ , and  $^{208}\text{Pb}(p, p)$  at  $E_p = 295$  MeV to obtain improved neutron densities and radii from the experimental cross section data. The reaction calculation of  $\text{Pb}(p, p)$  at  $E_p = 295$  MeV was performed using RIA with the effective  $NN$  interaction of the ddMH model. For the target Pb density, the theoretical densities of the RHB (me2 and pc1) and SHFB (SKM\* and SLy4) calculations of spherical nuclei and the experimental SOG-fit densities are used as inputs of the reaction calculations.

The isotopic differences of the neutron density  $D(\rho_n)$  and radius  $D(r_n)$  of  $^A\text{Pb}$  from the reference  $^{208}\text{Pb}$  were investigated, and the isotopic ratio  $R(\sigma)$  of  $^A\text{Pb}(p, p)$  to the  $^{208}\text{Pb}(p, p)$  cross sections was analyzed. The cross sections are sensitive to the profile of the surface-neutron density but insensitive to the internal density. In the analysis of  $D(\rho_n)$ , the SOG-fit density was found to have a flapping behavior of  $4\pi r^2 D(\rho_n)$  in the internal region,

causing an artificial increase of the neutron radius of  $^{208}\text{Pb}$  that was inconsistent with theoretical predictions.

A further detailed analysis was performed with the hole model by assuming a  $^{208}\text{Pb}$  core and neutron-hole contributions for the neutron densities of  $^{204}\text{Pb}$  and  $^{206}\text{Pb}$ . A clear correspondence between the surface-neutron density and the  $(p,p)$  cross sections was clarified; the oscillation amplitudes of  $R(\sigma)$  is determined by the isotopic neutron radius difference  $D(r_n)$ , whereas the central values of the oscillation of  $R(\sigma)$  are sensitive to the surface-neutron density around the peak position of  $4\pi r^2 \rho_n(r)$ . Because of this correspondence between the isotopic structure differences ( $D(\rho_n)$  and  $D(r_n)$ ) and the isotopic cross-section ratio  $R(\sigma)$ , the  $D(\rho_n)$  and  $D(r_n)$  values can be safely extracted from the observed  $(p,p)$  data with less model dependence. By fitting the experimental  $R(\sigma)$  with the hole model,  $D(r_n) = -0.012$  fm with the acceptable range  $D(r_n) = -0.03 \sim -0.006$  fm was obtained for  $^{206}\text{Pb}$ . Furthermore, the improved neutron densities of  $^{204}\text{Pb}$ ,  $^{206}\text{Pb}$ , and  $^{208}\text{Pb}$  were reconstructed from the SOG-fit density using the  $D(\rho_n)$  obtained by hole-model analysis. The improved neutron densities of Pb isotopes successfully reproduced the experimental Pb( $p,p$ ) data measured at 295 MeV, including the isotopic cross-section ratio and the cross sections and analyzing powers. The results for  $r_n$  and  $\Delta r_{np}$  obtained by the improved neutron densities are reasonable values within the experimental errors and show smooth changes in a series of Pb isotopes from  $^{204}\text{Pb}$  to  $^{208}\text{Pb}$ .

It should be noted that the present results for  $D(r_n)$  and  $D(\rho_n)$  can be improved by a further precise analysis by taking into account experimental errors in the angular resolution and the possible reduction of systematic errors in  $R(\sigma)$ , which were omitted in the present analysis. Reanalysis of the Pb( $p,p$ ) data at 295 MeV including isotopic systematics such as the  $R(\sigma)$  data is requested to extract a revised SOG-fit density from the  $(p,p)$  data at 295 MeV.

The model uncertainties in the structure and reaction calculations were discussed by comparing the results obtained by RIA calculation with the ddMH and MH effective  $NN$  interactions using various theoretical densities. The present method of isotopic analysis was shown to be a useful tool for extracting neutron densities and radii from the  $(p,p)$  cross sections in a series of isotopes with less systematic uncertainties from model dependences. The method can be extended straightforwardly to systematic analyses of neighboring nuclei, particularly for the  $(p,p)$  data measured experimentally with the same setup at the same facility, because systematic errors can be significantly reduced in the experimental data of the isotopic cross-section ratio. This can be a great advantage for determining the nuclear sizes of unstable nuclei from  $(p,p)$  data measured in inverse kinematics.

## Acknowledgments

This work was motivated by the recent work of Ms. Shiyo Enyo. in her master thesis. It was supported by Grants-in-Aid of the Japan Society for the Promotion of Science (Grant Nos. JP18K03617 and 18H05407) and by a grant of the joint research project of the Research Center for Nuclear Physics at Osaka University.

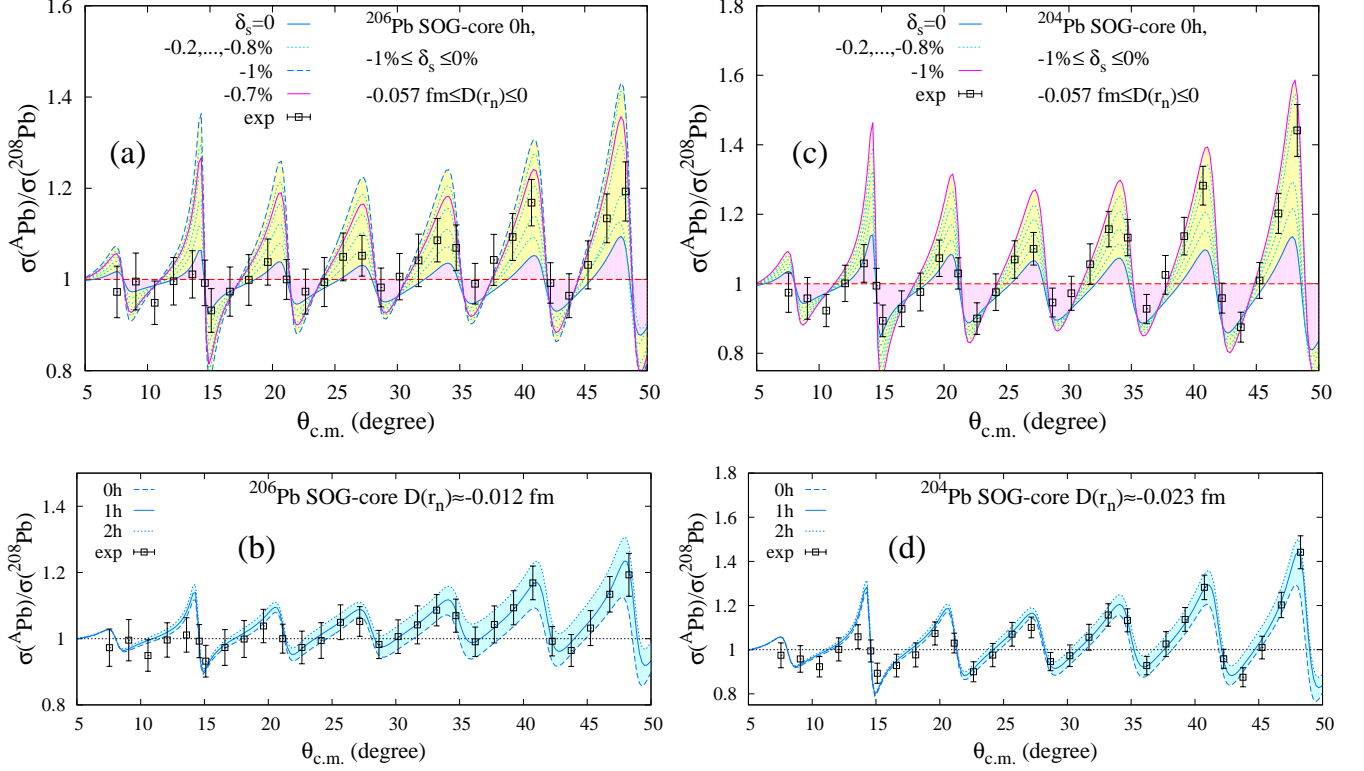


FIG. 16: Isotopic cross-section ratio  $R(\sigma)$  of  $^{A}\text{Pb}(p,p)$  to  $^{208}\text{Pb}(p,p)$  at 295 MeV, as calculated using the hole model with the SOG-fit core. Results for  $(0h, \delta_s)$  with  $-1.0\% \leq \delta_s \leq 0\%$  for (a)  $^{206}\text{Pb}$  and (c)  $^{204}\text{Pb}$ . Red lines show the results obtained using the  $(0h, -0.7\%)$  hole model with  $D(r_n) = -0.040$  fm of  $^{206}\text{Pb}$  and  $(0h, -1.0\%)$  hole model with  $D(r_n) = -0.057$  fm of  $^{204}\text{Pb}$ . (b)  $R(\sigma)$  of  $^{206}\text{Pb}$  obtained using the hole model with  $(0h, \delta_s = -0.2\%)$ ,  $(1h, \delta_s = -0.1\%)$ , and  $(2h, \delta_s = 0\%)$ , which give  $D(r_n) = -0.011$  fm,  $-0.012$  fm, and  $-0.012$  fm, respectively. (d)  $R(\sigma)$  of  $^{204}\text{Pb}$  obtained using the hole model with  $(0h, \delta_s = -0.4\%)$ ,  $(1h, \delta_s = -0.3\%)$ , and  $(2h, \delta_s = -0.2\%)$ , which yield  $D(r_n) = -0.023$  fm. The experimental values obtained from the  $(p,p)$  data [5] are also shown.

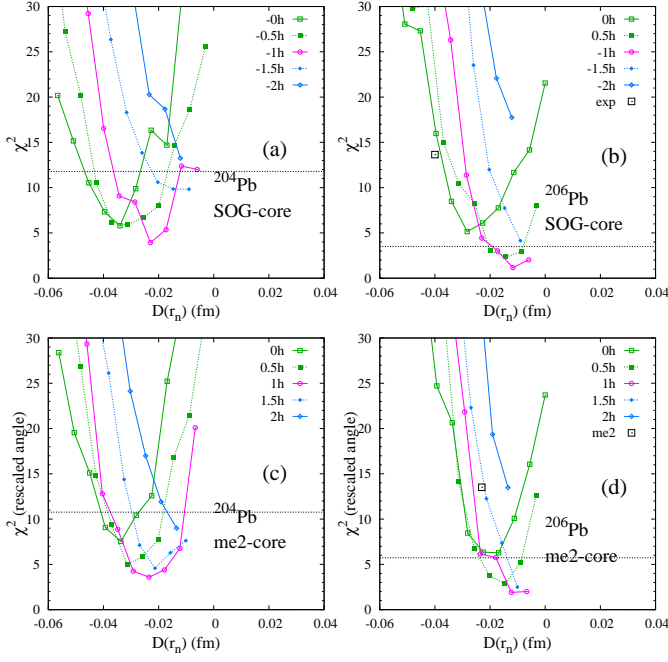


FIG. 17:  $\chi^2$  of  $R(\sigma)$  obtained by the ddMH calculation using the hole model with  $(0h, \delta_s)$ ,  $(0.5h, \delta_s)$ ,  $(1h, \delta_s)$ ,  $(1.5h, \delta_s)$ , and  $(2h, \delta_s)$  for  $\delta_s = \{0\%, 0.1\%, \dots -1.0\%\}$  for (a)  $^{204}\text{Pb}$  and (b)  $^{206}\text{Pb}$  with the SOG-core and (c)  $^{204}\text{Pb}$  and (d)  $^{206}\text{Pb}$  with the me2-core. The  $\chi^2$  values are plotted as functions of  $D(r_n)$ .  $\chi^2$  is calculated using 17 datapoints of the  $(p, p)$  data [5] excluding  $\theta_{c.m.} \leq 15.09^\circ$  at forward angles and  $\theta_{c.m.} = 21.13^\circ$ ,  $27.17^\circ$ ,  $28.67^\circ$ ,  $34.71^\circ$ , and  $42.24^\circ$  at dip angles. Rescaled angles  $\theta_{c.m.}^*$  are used for the me2 and hole model(me2-core) cases.

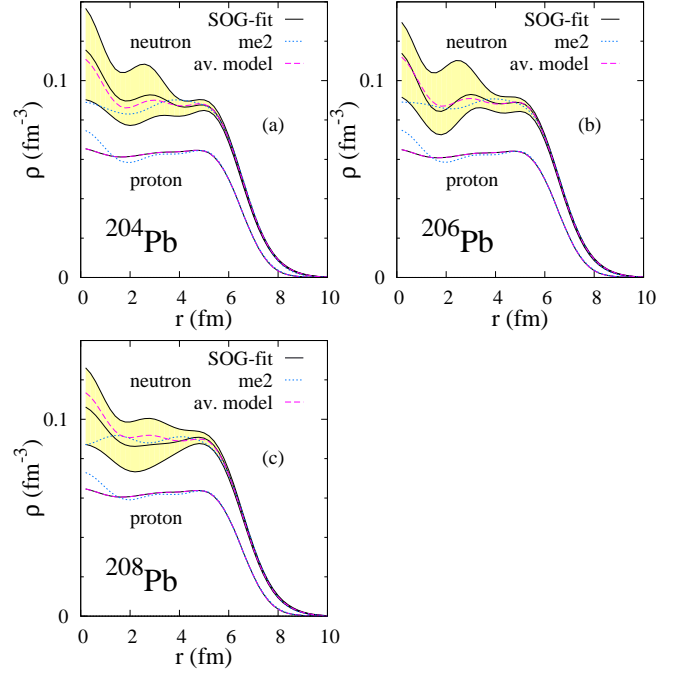


FIG. 18: Same as Fig. 1 but for the averaged-model densities compared with the me2 and SOG-fit densities.

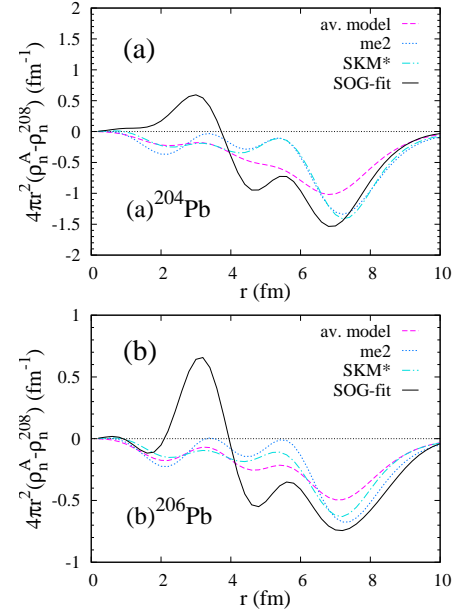


FIG. 19:  $4\pi r^2 D(\rho_n)$  for (a)  $^{204}\text{Pb}$  and (b)  $^{206}\text{Pb}$  of the isotopic neutron-density difference of the averaged-model densities compared with results of the SOG-fit, me2, and SKM\* densities.



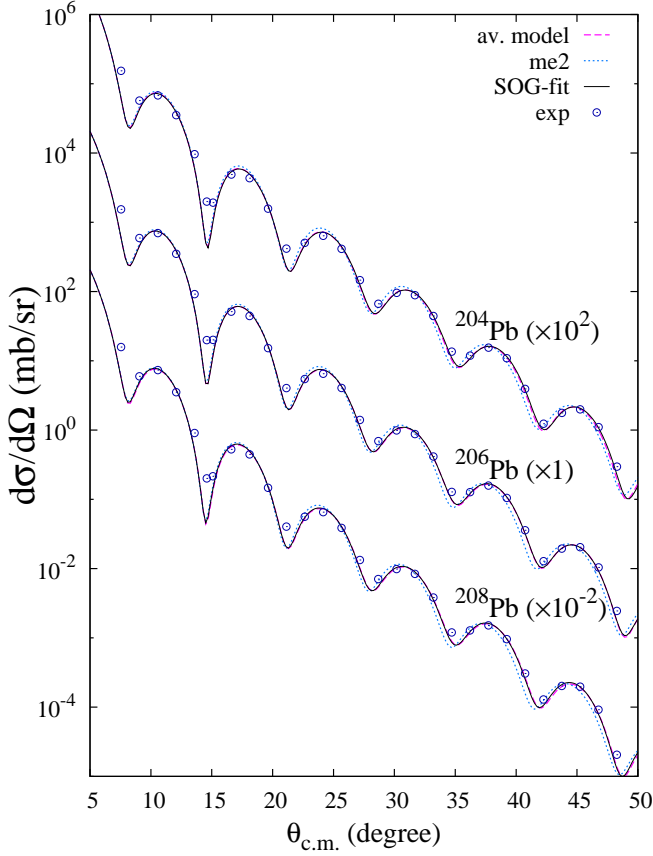


FIG. 20: Cross sections of  $\text{Pb}(p, p)$  at 295 MeV obtained via RIA with the ddMH model using the present averaged model, SOG-fit, and the me2 densities of Pb isotopes, together with the experimental data [5].

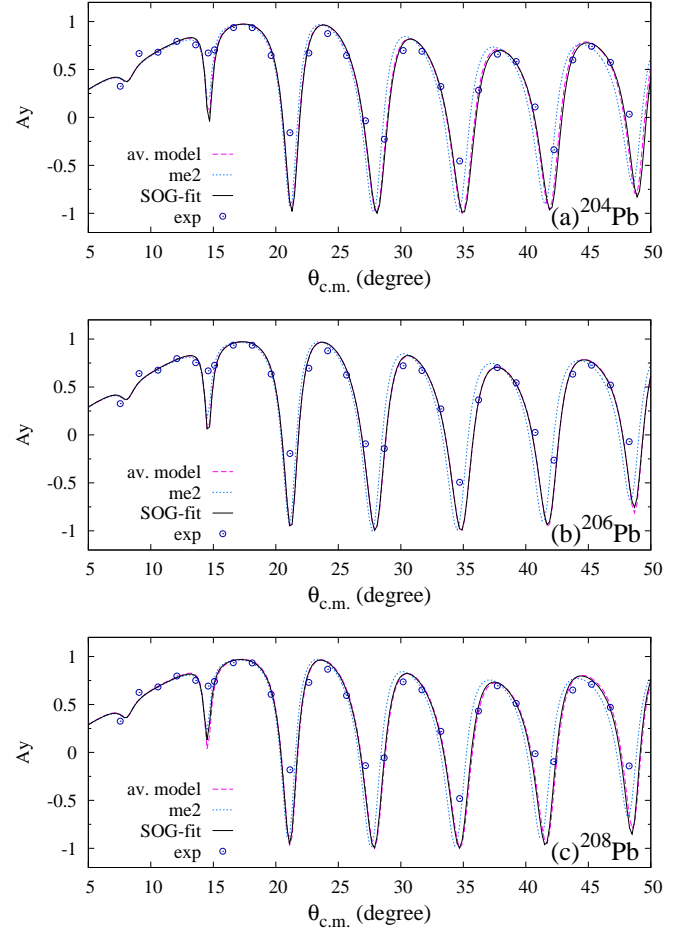


FIG. 21: Analyzing powers of  $\text{Pb}(p, p)$  at 295 MeV obtained by RIA with the ddMH model using the present averaged model, SOG-fit, and me2 densities of Pb isotopes, together with the experimental data from [5].

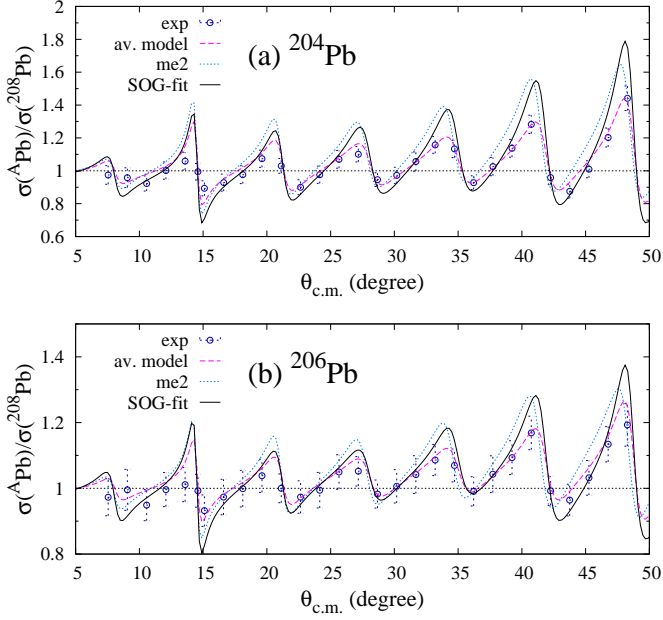


FIG. 22: Isotopic cross-section ratios  $R(\sigma)$  of (a)  $^{204}\text{Pb}(p, p)$  and (b)  $^{206}\text{Pb}(p, p)$  to  $^{208}\text{Pb}(p, p)$  at 295 MeV calculated using the present averaged model, SOG-fit, and me2 densities, together with the experimental values obtained from the  $(p, p)$  data [5].

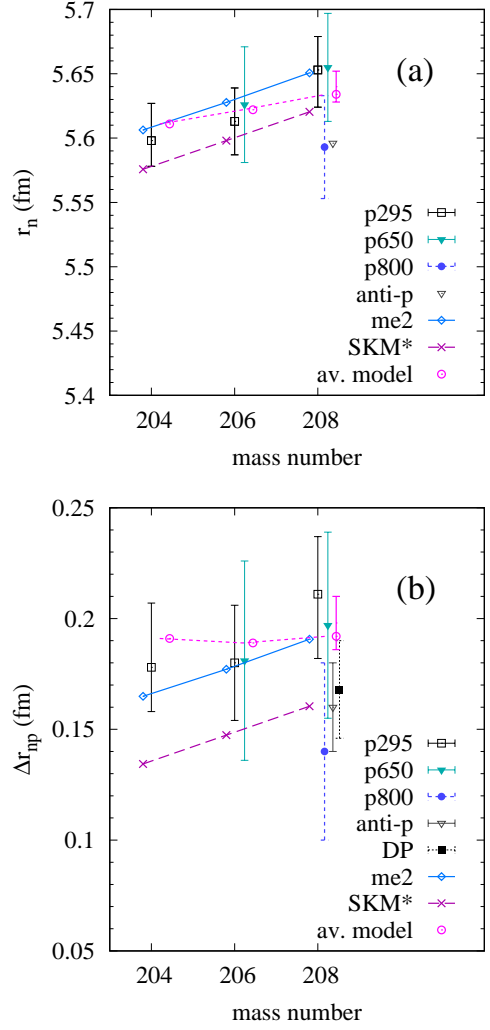


FIG. 23: Same as Fig. 2 but for the present result obtained by the averaged model (open circles) in comparison with the theoretical and experimental values. For  $^{208}\text{Pb}$ , the error range of the averaged model is roughly estimated using the acceptable range  $D(r_n) = -0.03 \sim -0.006$  fm obtained via the hole-model analysis and the  $r_n$  value of  $^{206}\text{Pb}$  of the averaged model.

### Appendix A: Equivalent $D(\rho_n)$ for the $(2f_{5/2})$ -hole model and the me2 densities

$D(\rho_n)$  and  $R(\sigma)$  obtained using the hole model of the  $(2f_{5/2})$ -hole configurations with the me2-core are shown in Fig. 24 (a) and (b), respectively. The equivalent  $(3p_{1/2})$ -hole-model density, which yields an approximately consistent result of  $R(\sigma)$  with the  $(2f_{5/2})$ -hole

model is obtained by tuning the parameters  $h$  and  $\delta_s$  of the  $(3p_{1/2})$ -hole model. The results obtained using the equivalent  $(3p_{1/2})$ -hole-model density adjusted to the hole model with the  $(2f_{5/2})^{-2}$  configuration are compared, In Figs. (c) and (d), the  $D(\rho_n)$  and  $R(\sigma)$  obtained using the equivalent  $(3p_{1/2})$ -hole-model density adjusted to the me2-density are compared with those of the me2-density.

- 
- [1] X. Roca-Maza, M. Centelles, X. Vinas, and M. Warda, Phys. Rev. Lett. **106**, 252501 (2011), arXiv:1103.1762 [nucl-th] .
- [2] X. Roca-Maza and N. Paar, Prog. Part. Nucl. Phys. **101**, 96 (2018), arXiv:1804.06256 [nucl-th] .
- [3] M. B. Tsang et al., Phys. Rev. C **86**, 015803 (2012), arXiv:1204.0466 [nucl-ex] .
- [4] V. E. Starodubsky and N. M. Hintz, Phys. Rev. C **49**, 2118 (1994).
- [5] J. Zenihiro et al., Phys. Rev. C **82**, 044611 (2010).
- [6] B. Klos et al., Phys. Rev. C **76**, 014311 (2007), arXiv:nucl-ex/0702016 .
- [7] S. Abrahamyan et al., Phys. Rev. Lett. **108**, 112502 (2012), arXiv:1201.2568 [nucl-ex] .
- [8] E. Friedman, Nucl. Phys. A **896**, 46 (2012), arXiv:1209.6168 [nucl-ex] .
- [9] C. M. Tarbert et al., Phys. Rev. Lett. **112**, 242502 (2014), arXiv:1311.0168 [nucl-ex] .
- [10] A. Tamii et al., Phys. Rev. Lett. **107**, 062502 (2011), arXiv:1104.5431 [nucl-ex] .
- [11] J. Piekarewicz, B. K. Agrawal, G. Colo, W. Nazarewicz, N. Paar, P. G. Reinhard, X. Roca-Maza, and D. Vretenar, Phys. Rev. C **85**, 041302 (2012), arXiv:1201.3807 [nucl-th] .
- [12] M. Centelles, X. Roca-Maza, X. Vinas, and M. Warda, Phys. Rev. C **82**, 054314 (2010), arXiv:1010.5396 [nucl-th] .
- [13] L. Ray, W. R. Coker, and G. W. Hoffmann, Phys. Rev. C **18**, 2641 (1978).
- [14] L. Ray, Phys. Rev. C **19**, 1855 (1979), [Erratum: Phys.Rev.C 20, 1212–1212 (1979)].
- [15] G. W. Hoffmann et al., Phys. Rev. C **21**, 1488 (1980).
- [16] C. J. Horowitz, Phys. Rev. C **31**, 1340 (1985).
- [17] D. P. Murdock and C. J. Horowitz, Phys. Rev. C **35**, 1442 (1987).
- [18] C. Horowitz, D. Murdock, and S. B.D., Computational Nuclear Physics 1, edited by K. Langanke, J. Maruhn, and S. Koonin (Springer-Verlag, 1991) p. 129.
- [19] H. Sakaguchi et al., Phys. Rev. C **57**, 1749 (1998).
- [20] S. Terashima et al., Phys. Rev. C **77**, 024317 (2008).
- [21] J. Zenihiro et al., (2018), arXiv:1810.11796 [nucl-ex] .
- [22] J. Piekarewicz and S. P. Weppner, Nucl. Phys. A **778**, 10 (2006), arXiv:nucl-th/0509019 .
- [23] S. Yoshida, H. Sagawa, J. Zenihiro, and T. Uesaka, Phys. Rev. C **102**, 064307 (2020).
- [24] X. Roca-Maza, M. Centelles, F. Salvat, and X. Vinas, Phys. Rev. C **78**, 044332 (2008), arXiv:0808.1252 [nucl-th] .
- [25] G. W. Hoffmann et al., Phys. Rev. C **41**, 1651 (1990).
- [26] T. Nikšić, N. Paar, D. Vretenar, and P. Ring, Comput. Phys. Commun. **185**, 1808 (2014), arXiv:1403.4039 [nucl-th] .
- [27] G. A. Lalazissis, T. Nikšić, D. Vretenar, and P. Ring, Phys. Rev. C **71**, 024312 (2005).
- [28] T. Nikšić, D. Vretenar, and P. Ring, Phys. Rev. C **78**, 034318 (2008), arXiv:0809.1375 [nucl-th] .
- [29] K. Bennaceur and J. Dobaczewski, Comput. Phys. Commun. **168**, 96 (2005), arXiv:nucl-th/0501002 .
- [30] J. Bartel, P. Quentin, M. Brack, C. Guet, and H. B. Hakansson, Nucl. Phys. A **386**, 79 (1982).
- [31] E. Chabanat, P. Bonche, P. Haensel, J. Meyer, and R. Schaeffer, Nucl. Phys. A **635**, 231 (1998), [Erratum: Nucl.Phys.A 643, 441–441 (1998)].
- [32] J. Zenihiro, Neutron density distributions of Pb deduced via proton e Ph.D. thesis, Kyoto University (2011).
- [33] H. De Vries, C. W. De Jager, and C. De Vries, Atom. Data Nucl. Data Tabl. **36**, 495 (1987).

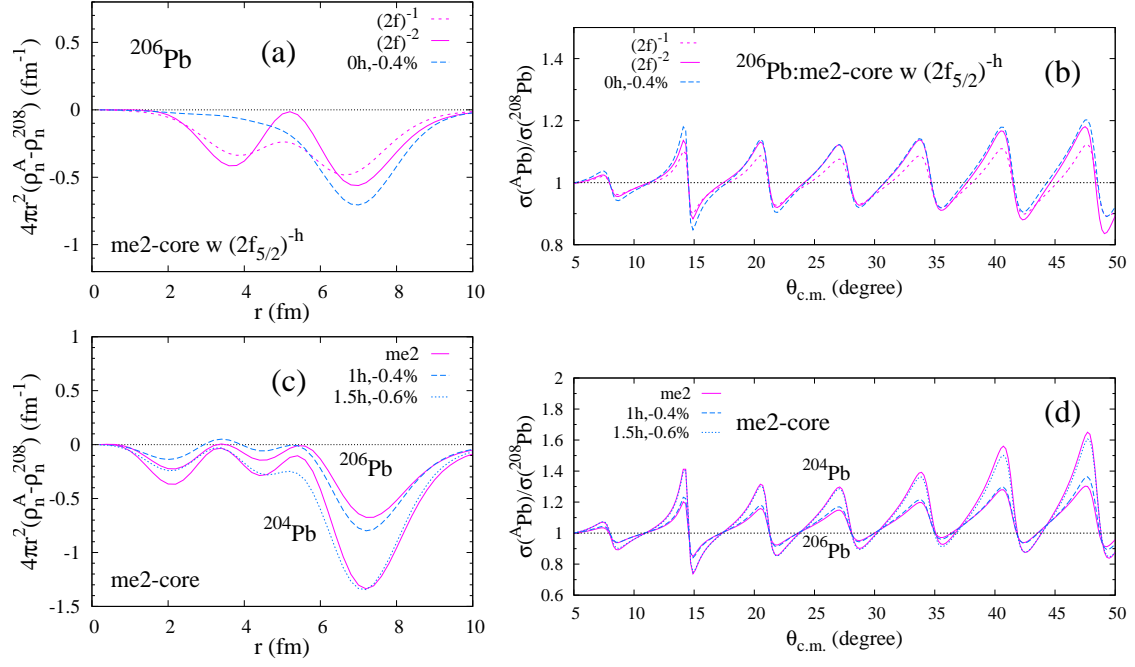


FIG. 24: (a)  $D(\rho_n)$  and (b)  $R(\sigma)$  obtained by the RIA+ddMH calculation using the hole model of the me2-core with  $(2f_{5/2})^{-1}$  and  $(2f_{5/2})^{-2}$  configurations (no scaling,  $\delta_s = 0$ ). The results obtained using the equivalent  $(3p_{1/2})$ -hole-model density with  $(0h, \delta_s = -0.4\%)$  that reproduces  $R(\sigma)$  of the  $(2f_{5/2})^{-2}$  configuration are shown for comparison. (c)  $D(\rho_n)$  and (d)  $R(\sigma)$  for the equivalent  $(3p_{1/2})$ -hole-model density, together with those for the me2-density. The adjusted parameters for the equivalent  $(3p_{1/2})$ -hole-model density are  $(1h, \delta_s = -0.4\%)$  for  $^{206}\text{Pb}$  and  $(1.5h, \delta_s = -0.6\%)$  for  $^{204}\text{Pb}$ .